Radiometric and Geometric Calibration of an Inexpensive LED-Based Lidar Sensor

by

Jordan Laughlin

A thesis submitted to the Department of Civil and Environmental Engineering,

Cullen College of Engineering

in partial fulfillment of the requirements for the degree of

Master of Science

in Geosensing Systems Engineering

Chair of Committee: Craig Glennie

Committee Member: Preston Hartzell

Committee Member: Hyongki Lee

Committee Member: William Wright

University of Houston

May 2020

Acknowledgments

Three parties must be recognized that without the support of, this research would not exist. First, I recognize Lieutenant Colonel William Wright, Colonel Mark Read, the United States Military Academy at West Point, and the US Army for providing me the time and financial support to complete this research. Second, I appreciate the tremendous support Preston Hartzell and Craig Glennie provided with their countless recommendations and guidance that significantly improved my work. Lastly, I thank my wife Jen for her everlasting support.

Abstract

Radiometric calibration of traditional lidar sensors that employ direct time of flight or phase-based ranging is well established. However, emerging inexpensive, lightweight, short-range lidar sensors that utilize non-traditional ranging methods report measurements that are not appropriate for existing radiometric calibration techniques. One such sensor, the TeraRanger Evo 60m by Terabee is a light emitting diode (instead of laser) lidar sensor with an automatically varying collection rate. This thesis investigates the performance of a new radiometric calibration model, one based on a neural network, applied to the Evo 60m. Application of the proposed radiometric calibration model resulted in performance similar to traditional lidar sensors, with mean differences in reflectance of no more than 5% and root mean square errors of no more than 6% for non-specular targets. The radiometric calibration model provides a generic approach that may be applicable to other low-cost lidar sensors and is a potential stepping stone toward development of a low-cost, multiple wavelength (multispectral) lidar sensor. The ranging performance of the Evo 60m was also evaluated in this work. Three of the four sensors evaluated fall below the manufacturer's stated accuracy level of ±40 millimeters while one lies just above the threshold at ±43 millimeters.

Table of Contents

List of Tables

List of Figures

1. Introduction

The use of light detection and ranging (lidar) for precise distance measurements within the geomatics discipline is traced to Erik Bergstrand's work in the late 1930s through the 1950s, where a known value for the speed of light was used to accurately determine range to a reflecting target (Bergstrand 1949). Bergstrand's method was conceptually similar to the one used for determining the speed of light at the time, where a modulated light source was directed at a reflecting target at a known distance. The phase of the return energy was then measured and used to compute the transit time, and hence velocity, of the light. Bergstrand reversed this concept by using a known value for the speed of light and subsequently using the measured phase to compute the distance to the target.

After their discovery in the 1960s, lasers were rapidly integrated into lidar instruments to take advantage of their more efficient, focused optical power characteristics compared to existing incoherent light sources (Maiman 1960; NOAA 2007). Today, laser-based lidar sensors are common for distance measurement, present on instruments ranging from affordable handheld devices used in the construction industry to spaceborne sensors that measure topography on a global scale (Wandinger 2006; Wehr and Lohr 1999). Lidar sensors are often combined with scanning devices to collect broad swaths of data from terrestrial or airborne platforms and are commonly referred to as laser scanners in this form. Laser scanners allow for the computation of 3D point locations for each measurement by combining range measurements with their associated angular measurements from the scanning device, thus building up a dense cloud of points representing the observed scene or object.

1.1. Low-Cost Lidar Sensors

Traditionally, laser-based lidar sensors have been expensive to purchase and maintain. Due to this, alternative light sources, such as structured light (Li 2014; Melexis 2017) or light emitting diodes (LEDs) (Koyama and Shiina 2011), have been used to develop more economical lidar sensors. These inexpensive sensors typically have a very short range (less than 5 meters), are often challenged in ranging accuracy and precision, and do not report target radiometric information. However, the small size and light weight of these sensors allow for many applications such as navigation systems for drones or robotics, small area mapping, industrial automation, and structural inspection (GrindGPS 2015; Corrigan 2019).

Particularly for LED-based lidar sensors, a key difference from laser-based lidar is the relatively wide field of view (FOV) due to the incoherent light source. Although typically viewed as a limitation, this wide FOV can be an ideal characteristic for proximity sensing or irregular object detection. Another key difference from traditional topographic lidar sensors is the departure from range determinations based on direct time of flight or phase difference measurements. Instead LED-based lidar sensors indirectly measure time of flight by relating integrated return energy measurements from a modulated LED light source to the distance of the reflecting target.

Recently, a LED-based lidar sensor with an advertised range of up to 60 meters was made commercially available – the TeraRanger Evo 60m by TeraBee. The sensor is economically priced at under $150, features an automatically varying measurement collection frequency up to 240 hertz, and has the potential to be adapted with different wavelength LEDs (Jan Kovermann, personal communication, 23 March 2018). This

creates the potential for an inexpensive multi-wavelength (i.e., multispectral) lidar system capable of providing rich target spectral information independent of solar illumination at a low cost.

1.2. Radiometric Calibration

Target spectral information is contained in the quantity of optical power returned to an illuminating lidar sensor from the observed target. The measurements of this optical power reported by a lidar sensor are typically referred to as ‘intensity’ values, and are a function of target material, target range, and sensor optical characteristics. Applications using lidar intensity, such as point cloud segmentation and target classification, are improved by radiometrically calibrating intensity values to a physical quantity tied to the observed target, e.g., reflectance or cross section (Höfle and Pfeifer 2007).

However, the difference in ranging methodology between traditional laser-based lidar sensors and low-cost LED lidar sensors results in a different set of reported observables. For example, in addition to range, the Evo 60m is capable of reporting ambient light, integration time (a variable that is a function of the ranging method) and return signal amplitude (intensity). The return signal amplitude is similar to traditional lidar intensity values but is characterized by large discontinuities corresponding to changes in integration time, which fluctuates in response to ambient light levels, target reflectance, and target range. The complex interactions between the observables reported by the Evo 60m does not allow the application of traditional physical and empirical lidar radiometric calibration models, and therefore requires development of a new approach.

1.3. Objective and Contribution

The primary objective of this thesis is to radiometrically calibrate a low-cost, indirect

time of flight, LED-based lidar sensor – the TeraRanger Evo 60m – to extend the value found in traditional lidar intensity values to this non-traditional lidar sensor. The ranging accuracy and precision of the Evo 60m is also examined with respect to ranges obtained from an instrument of higher accuracy and precision to provide a more complete characterization of the sensor.

The proposed radiometric calibration model approach is based on a simple neural network and may be extensible to other low-cost lidar sensors that do not report traditional, smoothly varying intensity values. To the author's knowledge, radiometric calibration of the Evo 60m, or any similar LED-based lidar sensor, has not been reported in literature or applied in a commercial setting. Successful radiometric calibration of the Evo 60m also represents a step towards creation of a low-cost multispectral lidar sensor. Finally examining the range performance of the sensor (i.e., geometric calibration) will augment the manufacturer's published specifications and provide relevant information to end users for making informed decisions on potential applications of the sensor.

2. Background

2.1. Lidar Measurement Techniques

The two most common lidar techniques, time of flight and continuous wave phase differencing, are briefly reviewed to provide context to the discussion of the indirect time of flight (ITOF) lidar technique used by the Evo 60m. The ITOF technique relies of observations of phase but, performs the measurements and calculations differently than the classical approach used by continuous wave phase differencing. Additional lidar measurements, such as triangulation and structured light, are not discussed as they are not directly relevant to this work.

2.1.1. Time of flight

Time of flight is the most common range determination method for lidar systems (Baltsavias 1999; Wehr and Lohr 1999; Shan and Toth 2009; Vosselman and Maas 2010). Time of flight ranging uses a precise timer to measure the time between a pulse of light's emittance and return. Range, z, is determined as

$$z = \left(\frac{c}{n}\right)\frac{t}{2}, \tag{1}$$

where c is the speed of light, t is the two-way time of flight, and n is the refractive index of the transmitting medium. Limitations of this method include the precision of the timer and the ability to identify a consistent location on the emitted and return pulse temporal profiles. This method is primarily used for long distance measurements where centimeter-level precision is acceptable.

2.1.2. Continuous Wave Phase Differencing

Continuous wave phase differencing is the second most common range determination

technique (Baltsavias 1999; Wehr and Lohr 1999; Shan and Toth 2009; Vosselman and Maas 2010). Range is determined by measuring the difference in phase between a continuously emitted light source, which is modulated with a relatively long wavelength, and the returned energy. The range is determined as

$$z = \frac{1}{4\pi}\frac{c}{f}\varphi\,, \tag{2}$$

where c is the speed of light, f is the frequency of the modulating wave, and φ is the phase difference. The phase difference is measured by comparing the emitted signal with the return signal (Vosselman and Maas 2010). The precision of this method corresponds to the resolution of the electronics and the modulating wavelength. The maximum target range that can be determined without ambiguity (i.e., an unknown number of cycles between the instrument and target) is half the modulating wavelength. In order to increase the maximum measurable distance but retain the precision associated with a shorter wavelength, multiple wavelengths can be modulated onto the emitted light. The phase measurements of the longer wavelengths are used to remove distance ambiguity associated with the shorter, but more precisely measured, wavelength. Stationary terrestrial laser scanners often use this method where millimeter-level precision is desired.

2.1.3. Indirect Time of Flight

ITOF determines distance through the indirect measurement of phase delay (Bellisai et al., 2011; Charbon 2014; Li 2014; Melexis 2017; Perenzoni and Stoppa 2011). Both continuous wave phase differencing and ITOF rely on the principle of determining range from the phase delay of the return signal, but the two methods differ based on how they determine that phase delay. Instead of measuring phase delay through continuous, direct comparison with the emitted signal, ITOF relies on a quadrature sampling, which is the

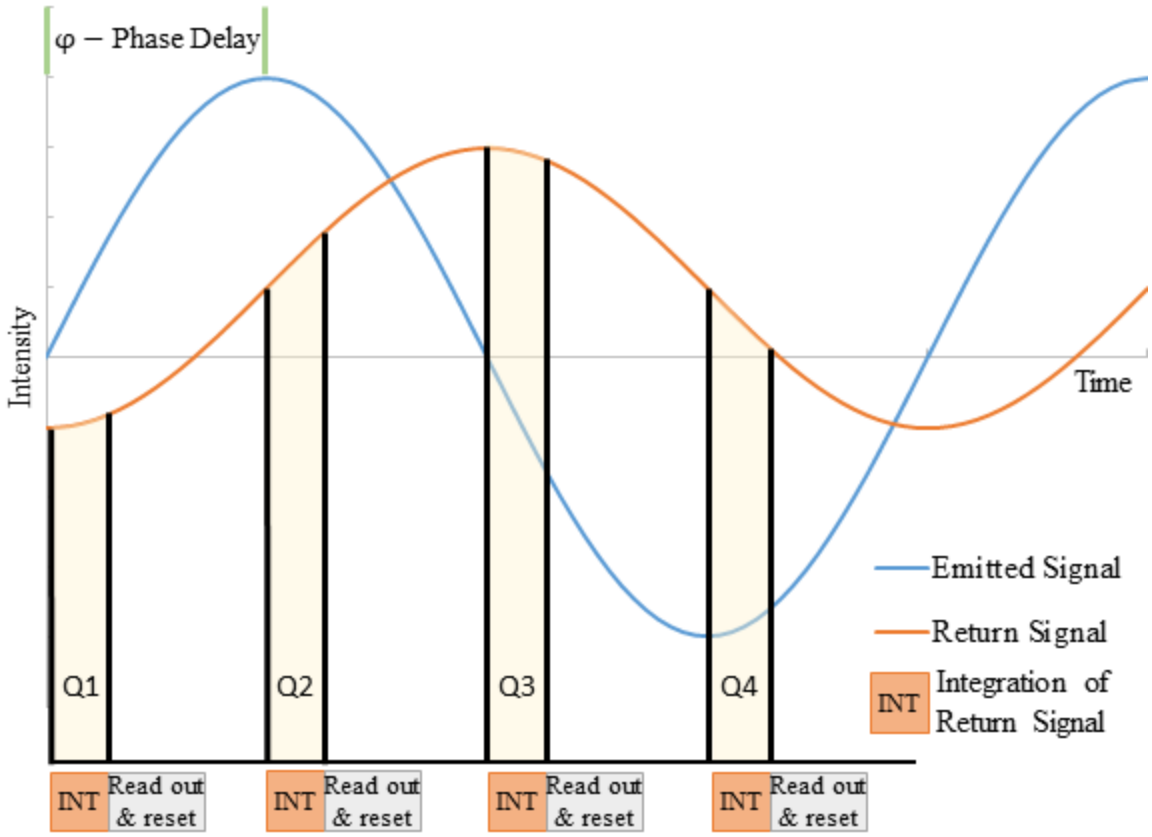

Figure 1 – Phase Determination for Indirect Time of Flight using Quadrature Sampling. Note that the return signal is offset due to background light and has decreased in amplitude due to the reflectance of objects in the scene.

integration of return energy four times per period, i.e., at 90-degree intervals. This is illustrated in Figure 1. Phase delay is then computed from these samples using

$$\varphi = tan^{-1}\left(\frac{Q4 - Q2}{Q1 - Q3}\right), \tag{3}$$

where $Q1 - Q4$ are the four sample readings (Bellisai et al., 2011; Charbon 2014; Li 2014). Range is then calculated using Equation (2). Additionally, amplitude, A, and background light (i.e. combination of ambient light and the sensor's emitted light), B, of the return signal is calculated as

$$A = \frac{\sqrt{(Q4 - Q2)^2 + (Q1 - Q3)^2}}{2} \text{ and} \tag{4}$$

$$B = \frac{Q1 + Q2 + Q3 + Q4}{4}. \quad (5)$$

(Li 2014) demonstrates the variance of an ITOF lidar range is dependent upon the amplitude and ambient light and is given as

$$\sigma = \frac{c}{4\sqrt{2}\pi f}\frac{\sqrt{A+B}}{c_d A}, \quad (6)$$

where c_d is modulation contrast, which describes the sensor's capacity to measure the phase shift of the incident light with respect to the modulated signal, and f the frequency of modulation. This indicates that a higher amplitude (strength of the returning signal), lower ambient light and a higher frequency is preferred. As with continuous wave phase differencing, the maximum target distance without ambiguity is half the modulating wavelength. This measurement technique can be implemented on single-pixel sensors such as the Evo 60m or multi-pixel sensors (Charbon 2014).

2.2. Radiometric Calibration

As previously noted, many sensors provide an intensity value in addition to range. Intensity is a unit-less and arbitrarily scaled quantity that is proportional to the power of the return signal received by the lidar sensor. Intensity values correspond to target reflectivity, but are also influenced by target range, orientation, and roughness, thus complicating their application to target characterization (Wagner et al., 2006; Wagner 2010). Intensity values can be radiometrically 'corrected' by normalizing for range but still lack a physical unit. Radiometric 'calibration,' however, transforms the intensity value to a physically meaningful quantity, such as reflectance. This increases the utility of the lidar intensity data as it can then be compared to values from different sensors (e.g. a spectroradiometer measurement) or from different collection campaigns. Radiometric

calibration is reviewed in the following sections starting with a brief discussion of light scattering and followed by a review of physical and empirical radiometric calibration models.

2.2.1. Scattering Theories

Historically, two distinct approaches have been used to describe the scattering of electromagnetic radiation – radiative transfer for passive sensors operating in the optical spectrum and electromagnetic theory for radar applications (Wagner 2010; Wagner et al., 2006). Electromagnetic theory considers coherent light, which is applicable to laser-based lidar sensors. The basic quantity of electromagnetic theory is the target cross-section, which describes the scattering of an incoming electromagnetic wave by an object.

In contrast to electromagnetic theory, radiative transfer methods are primarily applied to incoherent light sources, e.g., solar energy, and therefore do not consider wave phenomena such as interference or refraction in a rigorous manner. Instead, a target's reflectance is considered to depend only on the geometric arrangement of the light source, target, and receiver. This gives rise to the basic quantity used to describe the scattering of light in radiative transfer theory, the bidirectional reflectance-distribution function. An in-depth review of these two approaches to scattering in the context of lidar applications, including simplifying assumptions that result in electromagnetic theory closely resembling radiative transfer theory is given in (Wagner 2010).

2.2.2. Radiometric Calibration - Physical Models

The power received by a lidar sensor is related to target characteristics, acquisition geometry, the atmospheric environment, and system characteristics. This relationship, often termed the lidar range equation is based on the radar range equation and

electromagnetic theory and is given by (Höfle and Pfeifer 2007) as

$$P_r = \frac{P_t D_r^2}{4\pi R^4 \beta_t^2}\, \eta_{sys}\, \eta_{atm} \sigma, \tag{7}$$

where P_t is the transmitted power, D_r is the diameter of the receiver aperture, R is the range, β_t is the laser beam width, η_{sys} is the system transmission factor, η_{atm} is the atmospheric transmission factor, and σ is the target cross section. Target scattering characteristics, reflectance, and area are contained within the target cross section as

$$\sigma = \frac{4\pi}{\Omega}\, \rho A_t\,, \tag{8}$$

where Ω is the solid angle of scattering, ρ is target reflectivity, and A_t is the target area. Assuming a large Lambertian target that intercepts the entirety of the transmitted power, Equations (7) and (8) can be combined and simplified to

$$P_r = \frac{P_t D_r^2 \rho}{4R^2}\, \eta_{sys}\, \eta_{atm} \cos\alpha, \tag{9}$$

where α the incidence angle. Noting that the difference (from unity) of the atmospheric transmission factor is often negligible due to the relatively short lidar ranges measured from terrestrial or low altitude airborne platforms, η_{atm} can be removed from Equation (9). Since the system parameters of a lidar system are typically constant, including the transmitted power, they can be represented by a single calibration constant,

$$C_{cal} = \frac{P_t D_r^2}{4}\, \eta_{sys}. \tag{10}$$

Substituting this calibration constant into equation (9) leaves,

$$P_r = \frac{\rho}{R^2}\, C_{cal}\, \cos\alpha. \tag{11}$$

Solving for target reflectivity, we arrive at

$$\rho = \frac{P_r R^2}{C_{cal} \cos \alpha}. \quad (12)$$

Thus, for large targets with Lambertian scattering characteristics, observed at normal incidence, and over short ranges, target reflectance is proportional to the received power and target range

$$\rho \propto P_r R^2. \quad (13)$$

If C_{cal} can be estimated from observations of targets with known reflectance values, Equations (12) and (13) form the basis for a simple radiometric calibration approach that is based on the physical model of lidar ranging.

2.2.3. Radiometric Calibration - Empirical Models

The use of the lidar range equation for radiometric calibration assumes the intensity quantity reported by the lidar sensor is linearly related to the received optical power. When this is not the case, as is often true for short range terrestrial lidar sensors, regression models (i.e., an appropriate function fit to the data) or lookup tables can be used to create a purely empirical radiometric calibration model, e.g. (Hartzell, Glennie, and Finnegan 2015; Kaasalainen et al., 2008). These empirical models are developed from range and intensity measurements of multiple calibration targets with unique, known reflectance values observed at multiple ranges. Reflectance values can then be retrieved from a regression model or interpolating from a lookup table, providing the variables in the collected calibration data (typically lidar range, intensity, and target reflectance) vary systematically and smoothly with one another.

For the work in this thesis, the measurements reported by the Evo 60m sensor (range, amplitude, integration time, ambient light) and target reflectance do not vary smoothly with one another, eliminating the use of a simple regression model approach. Direct

interpolation of the collected calibration data in 5D space also produced poor results. Therefore, use of a neural network to approximate the complex relationship between the reported observations and target reflectance, i.e., empirical model based on a neural network, is proposed. Background information on neural networks is given in Section 3.4.1 to provide context to the network design methodology.

2.3. Geometric Calibration

In terms of the work in this thesis, geometric calibration is the verification of the Evo 60m's distance measurements against corresponding standard (known) distances, thereby providing an understanding of the uncertainties associated with the range measurements (Taylor and Kuyatt 1994). Since the Evo 60m measures only range (i.e., it is not a laser scanner where the lidar sensor is swept across a range of horizontal and vertical angles) the calibration method is similar to the range calibration methods applied to electronic distance measurement units on survey instruments, where, in a known environment, measurements of range are collected to targets at multiple distances (Gordon et al., 2005). Comparison of these measured ranges to the known values allows determination of whether systematic error exists. Multiple models for systematic error exist, ranging from simple (offset and scale) to more complex (e.g., inclusion of periodic components) (Gordon et al. 2005; Lichti 2007). In addition to accuracy, measures of range repeatability, i.e., precision, is also of interest. (Wujanz et al., 2017) demonstrated that lidar range precision is influenced by the measurement's return amplitude in a systematic manner. The relationship between the precision of a range measurement and its amplitude was modeled through use of a power function, which is also examined in the work herein.

3. Materials & Methods

3.1. Sensor

3.1.1. Description

The Terabee TeraRanger Evo 60m, illustrated in Figure 2, is a LED based, solid-state lidar sensor that, as mentioned previously, uses the indirect time-of-flight method to

Figure 2 – TeraRanger Evo 60m

determine range. TeraBee markets the Evo 60m as a distance measurement sensor for use in automation, robotics, and the internet of things. As such, the sensor only provides a distance measurement in its standard configuration. However, by using an internal debugging command along with custom firmware provided by Terabee to the University of Houston, the Evo 60m can report additional measurements of return signal amplitude, ambient light, and integration time for a total of four variables.

The manufacturer provides basic specifications, shown in Table 1, for the Evo 60m including range accuracy and resolution, where resolution refers to the quantization (rounding) of the reported distance (Terabee 2017). A notable change in the range resolution and accuracy at a range of 14 meters is listed in the specifications, beyond which the sensor's accuracy and resolution are degraded. This characteristic is important as it significantly affects the analyses in this thesis. Another important sensor measurement

Table 1 – Sensor Specifications

Properties		
Operating Wavelength	950nm	
Size	29x29x22mm	
Weight	12g	
Measurement Principle	Indirect Time of Flight	
Range	0.5m to 60m	
Collection Rate	Up to 240Hz	
Field of view	1.7deg	
Approximate Cost	€124.00 (~$140.00)	
Error		
	<14m	>14m
Resolution	5mm	20mm
Accuracy	±40mm	1.5%

characteristic is the automatic adjustment of the sensor's integration time, and therefore its collection, in response to the strength of the return signal, which is impacted by target range and reflectance and ambient light. As a consequence of these step-wise, rather than smoothly varying, integration time adjustments, the amplitude versus distance curves typically used for empirical lidar radiometric calibration models exhibit significant discontinuities.

The Evo 60m is an 'always-on' sensor, meaning that immediately after connecting the sensor to a power source it begins collecting measurements. Simultaneous use of multiple Evo 60m sensors, therefore, requires special care as the sensors will interfere with each other if aligned in the same direction. To eliminate this issue, the manufacturer provides a separate product to synchronize multiple sensors, although this product was not used in this work. Also noteworthy is that if the sensor's field of view spans two items of varying distances during a measurement, the sensor returns an averaged distance to the two objects rather than two distinct range measurements. Finally, although the Evo 60m's maximum range is listed as 60 meters, this is only achieved in optimal conditions, i.e., a highly

reflective target and low ambient light conditions (Terabee 2018). When the signal-to-noise ratio is too low, due to a large distance, low target reflectance, or high ambient light levels, the sensor reports a distance measurement of '-1'.

A single Evo 60m was purchased in May 2018. In order to evaluate the consistency between sensors, particularly in the calibration models and parameters generated in the work reported in this thesis, three additional sensors were purchased in May 2019. All four Evo 60m sensors were used throughout this work to test the repeatability of results between sensors.

3.1.2. Sensor Alignment

Field of view alignment (i.e., knowledge of where the sensor is 'pointing') is difficult for a lidar sensor operating in the non-visible spectrum, particularly for distances further than a few meters. The Evo 60m, unlike a laser scanner, provides no point cloud that can be examined, nor does it provide a visual indicator such as a reference dot or aligned sight. Given that many of the targets to be illuminated by the Evo 60m are not large (i.e., not all targets will be a wall several meters in width and height) it is important to have knowledge of the sensor's orientations to ensure valid measurements. Towards this end, a mount was constructed that enables the alignment of the four Evo 60m sensors with a Leica Disto laser distance meter (model E7400x), which emits a visible red laser beam.

The mount consists of an aluminum plate, two survey tribrachs, two angle brackets, four 3d-printed sensor brackets, and various attachment hardware as shown in Figure 3. The mount not only maintains the alignment of the four sensors with the laser distance meter, but also provides the ability to adjust the horizontal and vertical viewing angles of the entire sensor suite via the bottom tribrach. The mount is attached to a small rolling

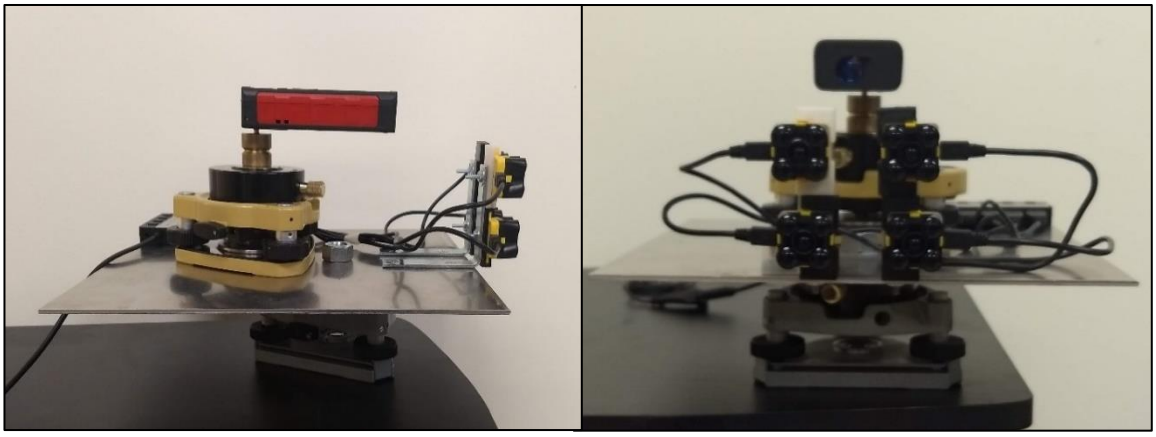

Figure 3 – Front and Side Views of Alignment Device

desk, allowing it to be easily moved to multiple ranges from a static target. After assembling the mount, the sensors were aligned with the Disto at a range of seven meters using an infrared-sensitive camera in a limited light environment. Seven meters was the longest range attainable with limited light in the Geosensing Systems Engineering Electronics Laboratory. For illustration purposes, Figure 4 shows the near infrared light pattern created by the four sensors at 1 meter range prior to fine alignment.

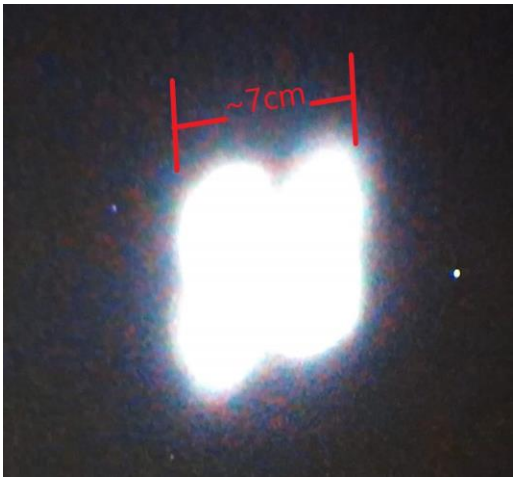

Figure 4 – Infrared Image of the Footprints of the Four Sensors at 1 meter

In addition to a visible laser that enables sensor alignment, the Leica Disto provides a reference range measurement at higher accuracy and precision than the Evo 60m sensors.

The manufacturer's specification for the Disto combines accuracy and precision together as 'measuring tolerance' listed as ±0.002 meter under normal operating conditions, which is an order of magnitude better than the quoted accuracy of ±0.040 meter for the Evo 60m. Ranges from the Leica Disto were compared to ranges measured with a Nikon NPL-322+ total station (used in reflector-less mode, accuracy listed as ±0.003 meter) and found to agree within ±0.002 meter.

3.2. Targets

Two groups of largely homogenous, flat materials were used as targets for calibration and validation of the radiometric models developed for the Evo 60m sensors. Due to the large sensor field of view (1.7 degrees), the reflectance standard panels currently possessed by the Geosensing System Engineering laboratory (12 inch/30.5 centimeter square) could not be confidently used at ranges of more than five meters. Five relatively large custom targets were, therefore, constructed from commonly available materials for the sensor radiometric calibration. A separate group of targets consisting of a variety of near-homogenous surfaces, existing both indoors and outdoors to maximize environmental conditions, was selected for validation of the radiometric calibration.

3.2.1. Calibration Targets

A reflectance standard suitable for use in calibration applications is spectrally uniform, Lambertian, and is of adequate size (Satterwhite and Allen 2003). Spectrally uniform refers to a flat spectral response with no absorption features. Since the LEDs used in the Evo 60m are centered in the near infrared at 950nm, the targets only need to be spectrally uniform in the immediate vicinity of this wavelength. A Lambertian surface is diffuse (not specular) and reflects incident optical power back to the illumination source according to the cosine

of the angle between the incident light and surface normal. Regarding the size of the calibration targets, the sensor footprint size along with a margin of error must be considered such that the emitted light will be fully intercepted by the target. Table 2 shows the footprint size for the Evo 60m from 1 to 60 meters. Finally, the reflectance standards should span as

Table 2 – Footprint Sizes

Range (meters)	1	5	10	15	20	60
Footprint Diameter (centimeters)	3	15	30	45	60	180

large a range of reflectance values as possible in order to capture the dynamic range of the sensor and to create a radiometric calibration model that is able to adequately predict a large range of target reflectance values.

To meet the requirements detailed in the prior paragraph, five 4x4 foot (1.22x1.22 meter) square panels of oriented strand board (OSB) were painted with multiple mixtures of white and black flat (matte) latex paint. The large panel dimensions comfortably accommodate the large sensor FOV beyond 20 meters (Table 2), and the matte paint finish was selected to maximize the Lambertian reflectance property. The spectral signatures of

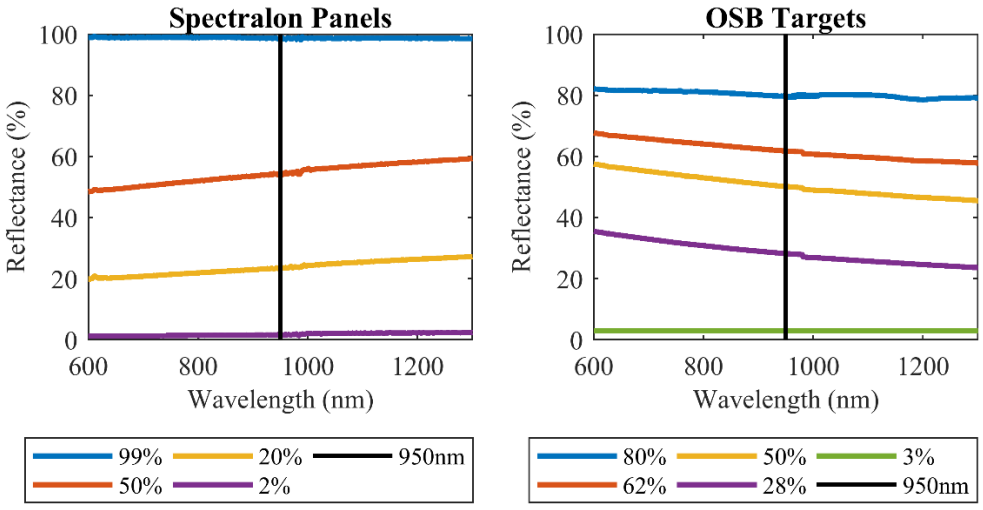

Figure 5 – Spectral Signatures for Spectralon® Panels (left) and Homemade OSB Calibration Targets (right)

the OSB targets were measured with a Spectra Vista Corporation spectroradiometer (model HR-1024 with 1024 channels and a range of 350nm-2500nm) using a Spectralon® 99% standard as the white reference. The five OSB calibration panels have unique spectral signatures ranging from 3% to 80% and exhibit a Lambertian response (validated in the results section of this thesis). Figure 5 shows the spectral signature of the OSB calibration targets alongside the signatures of the four Spectralon® standards. In retrospect, OSB is not recommended for future targets due to its heavy weight and textured surface properties. However, the uniformity of the painted OSB panel spectral responses is similar to the Spectralon® standards and, as will be illustrated later in this thesis, the painted OSB is highly Lambertian.

3.2.2. Test Targets

Twelve test targets of 'real-world' materials were selected to test the performance of

Table 3 – Test Target Observed Reflectance at 950nm

Material	Reflectance (%)
Black Foam	5
Gray Stucco Wall*	19
Gray Tabletop	36
Gray Painted Wall*	45
Red Brick*	46
Brown Paper	59
White Poster Board	84
Plywood	87
Silver Door*	54
Brown Door*	56
White Painted Wall	82
Corkboard	86

* Material Collected Outdoors

the radiometric calibration. These materials were found in naturally occurring conditions in both indoor and outdoor environments. Seven of these targets were indoors where the ambient lighting was able to be controlled with a halogen light source. The remaining five targets were outdoors and therefore subject to natural (solar) ambient light conditions. As with the painted OSB, each test target's reflectance was observed using a SVC spectroradiometer. The twelve target surfaces are shown in Figure 6 and their observed reflectance at 950 nm in Table 3.

Figure 6 – Test Targets (left to right, top to bottom): Black Foam, Gray Stucco Wall*, Gray Tabletop, Gray Painted Wall*, Red Brick*, Brown Paper, White Poster Board, Plywood, Silver Door*, Brown Door*, White Painted Wall, Corkboard.

*Material Collected Outdoors

3.3. Data Collection

Four collection campaigns were carried out to evaluate the Evo 60m. Each of the four

sensors collected data in each campaign. Fifty individual readings were collected for each unique collection, i.e., each unique combination of distance, ambient light level, target material, and incidence angle. These groups of 50 readings are hereafter referred to as a 'setup.' For each setup, the Leica laser distance meter determined the true, or standard, range. All data collection occurred in a dry environment. Details for each of the four collection campaigns follow.

3.3.1. Calibration Collection

The goal of the calibration campaign was to collect reliable and well distributed measurements – in target reflectance, range, and ambient light – for use as training data for a neural network. The data was primarily collected in an indoor environment with ambient light levels controlled by a halogen light source. Measurements were collected with each Evo 60m sensor at approximately every meter between 1 and 18 meters for three ambient light levels on each of the five OSB calibration targets. Additionally, measurements were collected outdoors in a very high ambient light environment (a clear, sunny day) over the same distance interval and target selection. It is noted here that the measurements collected under the very high ambient light conditions (outdoors) have gaps due the sensor's occasional inability to determine the range because of the low signal to noise ratio (very high ambient light overwhelms the sensor LED light output). This data was collected in June 2019 and consists of 15,400 unique measurements (308 setups) per sensor.

3.3.2. Test Collection

The purpose of the test campaign was to collect data for evaluating the trained radiometric calibration model. Measurements to the twelve test targets, which vary in size and composition were collected between 1 and 18 meters. The ambient light level also

varied, but in an uncontrolled manner due to cloud movement. This data was collected in June 2019 and consists of 15,000 unique measurements (300 setups) per sensor.

3.3.3. Temporal Test Collection

In order to examine the stability of the sensors, the same data as in the test collection, described above was acquired one month after the original collection. Data from two of the OSB calibration targets, 50% and 28%, was also acquired. The data was collected in August 2019 and consists of 25,600 unique measurements (512 setups) per sensor.

3.3.4. Incidence Angle Collection

In order to qualitatively evaluate the Lambertian scattering characteristic of the OSB calibration targets and several test targets that produced anomalous results, measurements were made with the incidence angle varied in ten-degree increments from 0 to 60 degrees. This collection was performed in an indoor environment where the ambient light was controlled. As the effect of the incidence angle was the primary focus, the target distance was kept approximately equal and the ambient light level held constant for each target. The ambient light was also kept at a low level to create a favorable environment for the sensor. The incidence angle data was collected in July 2019.

3.4. Radiometric Calibration

As stated earlier, a new model for radiometric calibration built on an artificial neural network is investigated in this thesis to accommodate the nonlinear and discontinuous nature of integration time and amplitude measurements reported by the Evo 60m. Neural networks are briefly reviewed in the following section, followed by a description of the methods used to design the neural network used for the radiometric calibration model.

3.4.1. Background on Neural Networks

Neural networks are non-linear statistical models determined using controlled observations (Hastie, Tibshirani, and Friedman 2009; Goodfellow, Bengio, and Courville 2016). There are two types of neural networks, supervised and unsupervised (Goodfellow, Bengio, and Courville 2016). Unsupervised neural networks are trained using an unlabeled dataset of only inputs and determines an output by identifying similar characteristics between the inputs. The outputs from an unsupervised network are then manually labeled. Supervised neural networks, which is the type used in this research, are trained using a labeled dataset where both inputs and outputs provided.

Supervised neural networks are typically grouped into two major categories, classification and function estimation (regression) (Hastie, Tibshirani, and Friedman 2009). A classification network's purpose is to categorize the input, often an image, into one of multiple possibilities. An example input is a picture of an animal that a classification network must evaluate as a cat, dog, or cow. The purpose of a function estimation network is to determine an output related to an input through an unknown function. This is primarily used when the function being approximated has too many unknowns to solve for a solution (Hastie, Tibshirani, and Friedman 2009). This is the category of neural networks used in this work.

Neural networks consist of three basic components: inputs, layers, and outputs (Hastie, Tibshirani, and Friedman 2009). Inputs are the measured quantities, outputs are the values to be determined, and layers each contain collections of nodes. These components can be connected (i.e., networked) in multiple ways. Three common architectures, illustrated in Figure 7, are: (1) feedforward, in which information flows from layer (or input) only to the

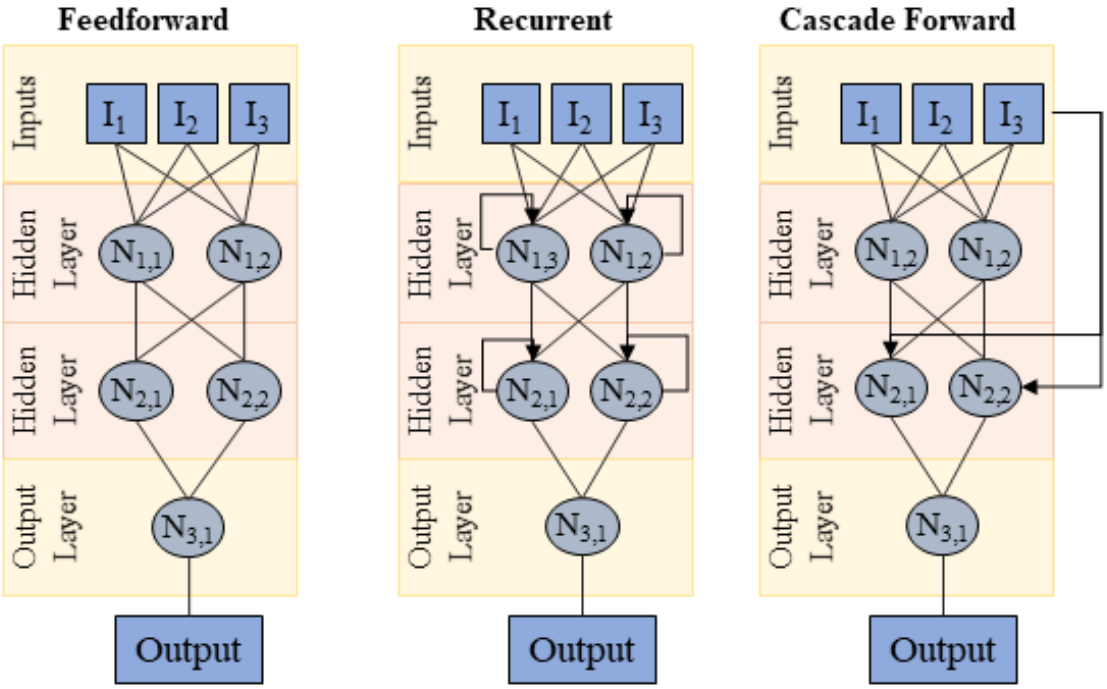

Figure 7 – Example Neural Networks (L to R) – Feedforward, Recurrent, Cascade Forward. The output is calculated using nodes, $N_{i,j}$, which are computed using values from the previous layer's nodes, inputs, I_i, or that node (for recurrent networks).

subsequent layer (or output), (2) recurrent, where the output of a node (or layer) is reprocessed through that node (or layer), and (3) cascade forward, where the inputs are connected to each hidden layer. This research focuses on a fully connected feedforward network, where fully-connected means all inputs, nodes, or outputs are connected between layers. Each of the network architectures were briefly tested with all the architectures producing comparable results. The feedforward network was selected as it is the least complex which, in turn, required fewer computing resources for training.

In a feedforward network, node values are a function of the previous layer's node values (or the inputs) in combination with weights that are assigned to each connection (Kriesel 2007). This relationship is illustrated in Figure 8, and expressed in equation form as

$$y = f\left(\sum_{i=1}^{n} X_i W_i + W_b\right), \tag{14}$$

where y is the computed node value, f is an activation function, X_i are node values from the prior layer (or inputs), W_i are the weights for each connection to the prior layer node values (or inputs), and W_b is the weight associated with the bias of that node. Note that the

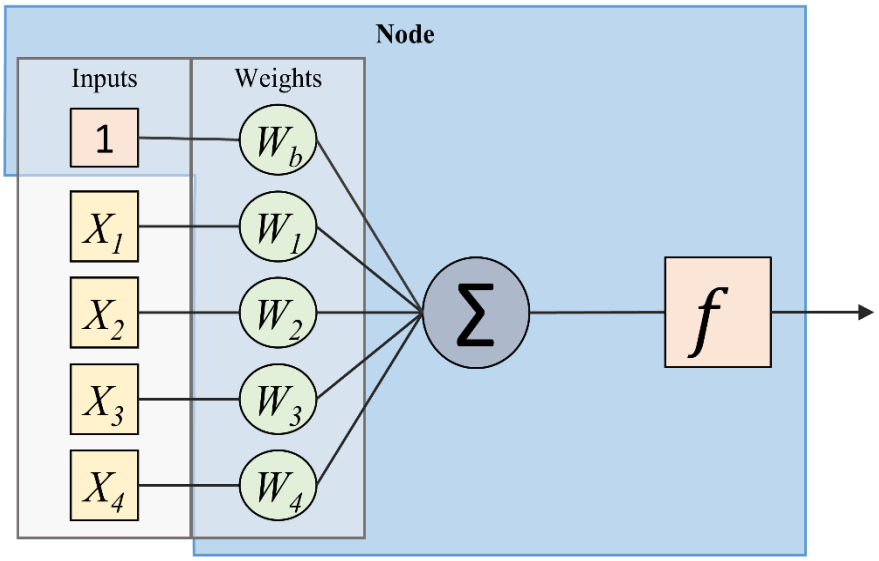

Figure 8 – Node Computation. The inputs, X_i, are multiplied by their corresponding weights, W_i, summed, and the sum is passed through the activation function f. Note the presence of the bias node input (value equal to 1) and bias node weight, W_b.

bias weight allows the resulting node value to be shifted for an improved fit (analogous to the y-intercept in a simple linear fit), and that the activation function transforms the weighted sum to a new value (activation functions are discussed in section 3.4.2.1). Since a layer is comprised of multiple nodes, their computations can be collected into a simple vector expression,

$$\begin{bmatrix} y_1 \\ \vdots \\ y_m \end{bmatrix} = \begin{bmatrix} f\left(\sum_{i=1}^{n} X_i W_{1,i} + W_{1,b}\right) \\ \vdots \\ f\left(\sum_{i=1}^{n} X_i W_{m,i} + W_{m,b}\right) \end{bmatrix}, \tag{15}$$

where *m* is the number of nodes within that layer. Note that all nodes within a layer use the same activation function.

The network weights are unknown parameters that must be optimized for the network to produce the desired output values. The weights are determined in an iterative process to minimize error, in this case mean squared error calculated by

$$\frac{1}{2m}\sum_{i=1}^{m}\left(\hat{y}^{(i)} - y^{(i)}\right)^2, \tag{16}$$

where *i* is the sample, $\hat{y}^{(i)}$ is the predicted value of the i-th sample, $y^{(i)}$ is the expected (known) value of the i-th sample and m is the number of samples. Some optimization algorithms, such as Bayesian Regularization, add a regularization term that penalizes large weights in order to mitigate overfitting. A model where some of the weights are very small effectively results in a simpler model with fewer nodes, which has the effect of preventing overfitting (Goodfellow, Bengio, and Courville 2016).

Optimization algorithms require training data to be separated, typically into three groups: train, validate, and test. Train data is used to optimize the network weights, referred to as training the network, to minimize error in the predicted outputs. Validation data is used to independently assess the network training progress and prevent overfitting by stopping training if the validation error increases (a.k.a. early stopping). Stopping network training can also be trigged by a set number of training epochs (an epoch is a complete iteration using all the training data), reducing the error metric below a specific threshold,

or when the change in weight values after an iteration update (i.e., step size) falls below a defined threshold. Once network training has stopped, the network configuration that produced the smallest validation error is used. For example, in Figure 9 this occurred at epoch 12. Test data is independent of the training process, and is used to evaluate the effectiveness of the network. Note that the test data group must be consistent to provide comparable results when evaluating multiple neural networks.

The initial values of the weights are usually set to random values. The optimization algorithm then adjusts these values to minimize the training data error. Gradient descent is

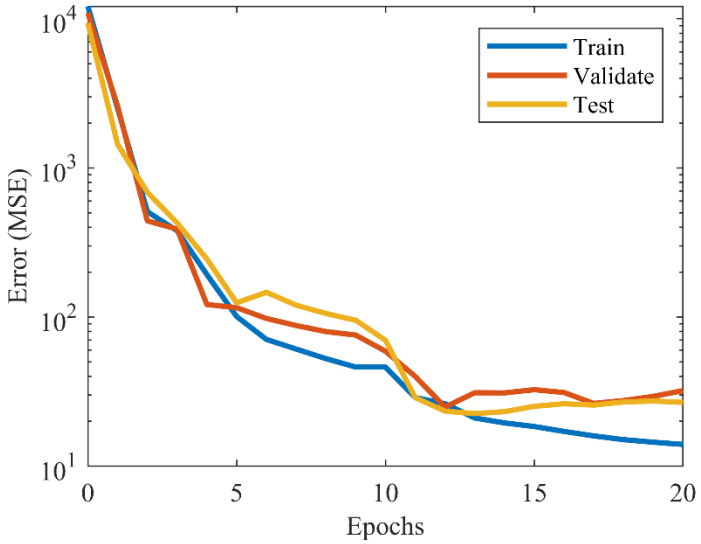

Figure 9 – Neural Network Training Error

a simple example of an optimization algorithm where updated weight values are determined via partial derivatives of the network error metric (e.g., Equation (16)) with respect to each unknown weight,

$$\Theta^1 = \Theta^0 - \alpha \nabla J(\Theta), \tag{17}$$

where Θ^1 is the next series of weights, Θ^0 is the current series of weights, α is the step size, and $\nabla J(\Theta)$ is the direction of fastest descent of the error surface determined using partial

derivatives. Many optimization algorithms are modifications of gradient descent, including those evaluated for use in this research (as discussed in the next section). Once the network weights have been optimized, the neural network can then be used to generate predicted output values from new input data.

3.4.2. Radiometric Calibration Model – Neural Network Design

A key strength of neural networks is their flexibility to model functions from simple to complex. This flexibility is seen in the numerous types (feedforward, recurrent, cascade, etc.), structural design possibilities (number of layers, number of nodes, activation function selection, etc.), and the choice of optimization algorithm. Consequently, the sheer number of design architectures, and the reality that multiple designs will likely achieve very similar results, is a challenge when developing a network. In order to determine an appropriate network design for the radiometric calibration model in this work, several design options were empirically evaluated. MATLAB® was used for the network design and analysis reviewed in the remainder of this section.

In terms of training data, the separation between train, validate, and test data groups was kept consistent throughout the network design process to provide comparable results. The train and validation data groups were filled with measurements from the calibration collection campaign. The validation data group was 10% of the calibration campaign measurements, separated by unique setup (i.e., a unique combination of distance, ambient light, and target), with the exception of Bayesian Regularization, which does not use a validation dataset. In this case, all of the collection campaign measurements made up the train data group. To evaluate the robustness of the model, the test data group was made up of 10% of the measurements from the test collection after excluding any surfaces assessed

to have specular properties (see section 4.2.2 for a discussion of specular targets), again separated by unique setup. The remaining 90% of measurements from the test collection were used in the analyses in Section 4 (Results and Discussion).

To begin the network design, a fully-connected feedforward network was selected due to the relative simplicity (four inputs and a single output) of the function being approximated. The following network design options were empirically evaluated: number of hidden layers, number of nodes within the layers, optimization algorithm choice, and activation function choice. These options are examined in the following subsections.

3.4.2.1. Optimization Algorithms and Activation Functions

Three optimization algorithms - Levenberg-Marquardt, Scaled Conjugant Gradient, and Bayesian Regularization - were considered. Briefly, the Levenberg-Marquardt (LM) algorithm combines both the gradient descent and Gauss-Newton minimization methods, shifting from gradient descent to the Gauss-Newton method as convergence slows. The LM algorithm is used on moderate sized problems and is a quick method of learning (Jazayeri, Jazayeri, and Uysal 2016; Gavin 2019). Scaled Conjugant gradient (SCG) was chosen as it is a classical optimization algorithm for neural networks. It is an improvement on the conjugant gradient method and uses a second order approximation to determine both the search direction as well as the step size (Møller 1990). Both the LM and SCG algorithms were set to terminate training when the validation results did not improve for six epochs. The Bayesian Regularization (BR) algorithm is known to be useful on noisy and difficult datasets (Jazayeri, Jazayeri, and Uysal 2016; Dan Foresee and Hagan 1997). In addition to minimizing the cost function, the BR algorithm eliminates weights with little impact to prevent overfitting. Since BR does not use a validation dataset, training was

terminated when either the gradient decreased below a threshold (set to be 10^{-7}) or 1000 training epochs.

A variety of hidden layer and node counts were used with the three optimization algorithms. The mean error for the top ten percent of performing networks for each optimization algorithm for one, two, and three hidden layers is shown in Figure 10. The

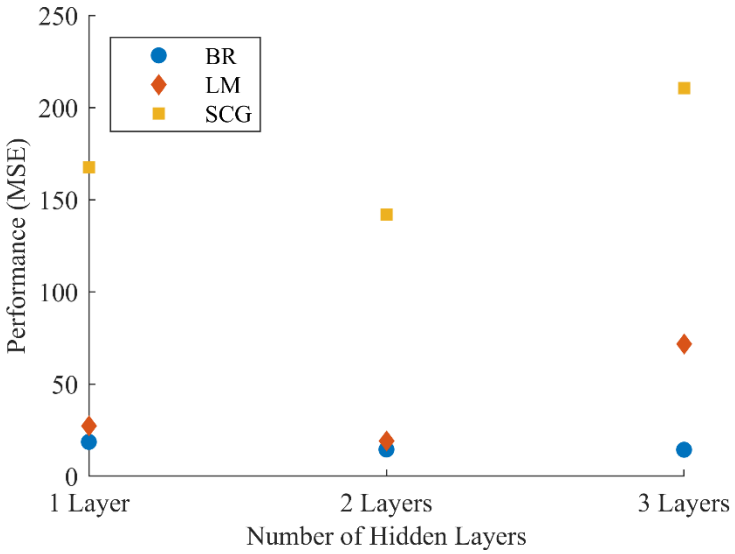

Figure 10 – Mean Best Performance by Hidden Layer

SCG algorithm performed the worst across all hidden layer numbers, while LM and BR methods were closely matched for one and two hidden layer models. A single hidden layer did not perform as well as two hidden layers and three hidden layers provides either worse results or results that were not notably better, depending on the optimization algorithm. Therefore, a two hidden layer network optimized using either the Bayesian Regularization or Levenberg-Marquardt algorithm is a good option for this application.

3.4.2.2. Activation Function

Six activation functions were tested: three step-wise linear functions and three

nonlinear functions of the sigmoid variety. Linear activation functions are frequently used due to their computational efficiency and limited complexity (Nwankpa et al., 2018). Three linear functions, shown in Figure 11, were selected: the positive linear (poslin), saturating

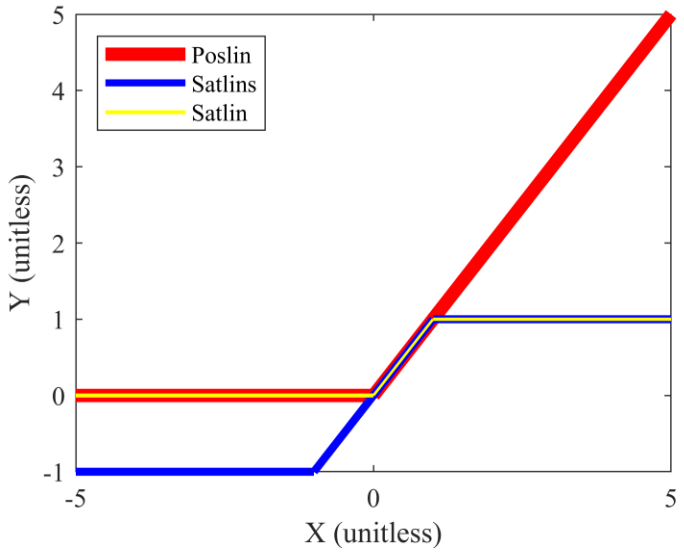

Figure 11 – Linear Family of Functions

linear (satlin), and symmetric saturating linear (satlins). Nonlinear sigmoid functions all exhibit an 'S' shaped curve and, in contrast to some of the step-wise linear functions, are

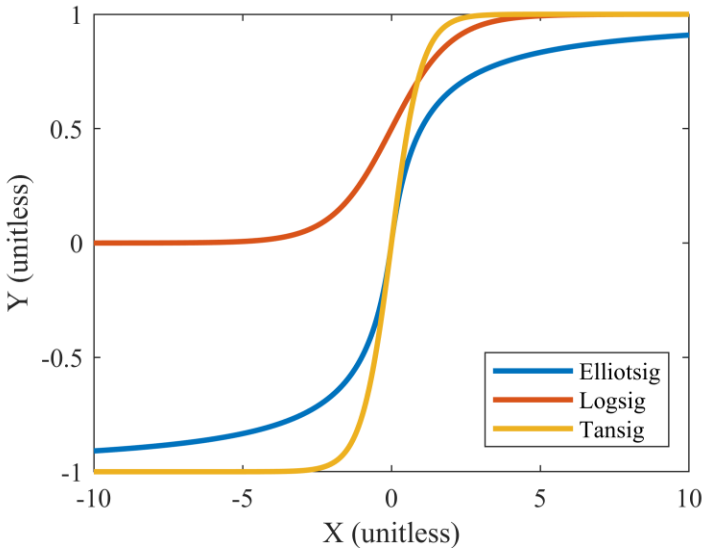

Figure 12 – Sigmoid Family of Functions

bounded and smoothly differentiable. Three sigmoid functions, shown in Figure 12, were selected: the Elliot symmetric sigmoid (elliotsig), log sigmoid (logsig), and hyperbolic tangent sigmoid (tansig) (Yonaba, Anctil, and Fortin 2010).

Using a process similar to that for selecting the optimization algorithm, multiple networks with a variety of node counts (between 1 and 20 for each layer) were trained for each activation function. The mean errors for the top ten percent performing combinations of activation function and node numbers are shown in Figure 13, where it is seen that the two best activation functions are logsig and tansig. Additionally, Bayesian Regularization

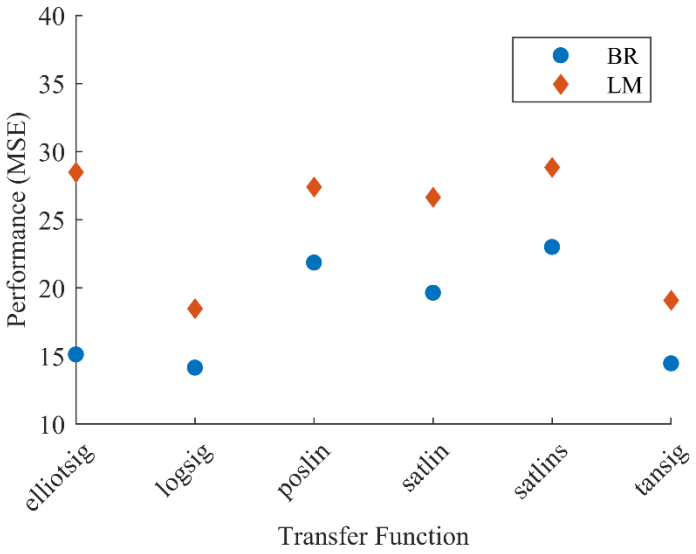

Figure 13 – Mean Best Performance by Activation Function

shows better performances across all activation functions. Therefore, the neural network design was further narrowed to either the logsig or tansig activation function and BR optimization.

3.4.2.3. Number of Nodes

The performance of the neural network as a function of the number of nodes in each of

the two hidden layers was examined next. Initially, an interval grid search for each activation function determined that the optimal number of nodes in each layer was less than 15. Following this, a continuous grid search was then performed (see Figure 14) the results of which suggest that node numbers in the range of 5-10 for each hidden layer are preferable. The randomness in the graphs in Figure 14 is due to the random initialization of the network weights at the start of training for each possible combination. It is likely

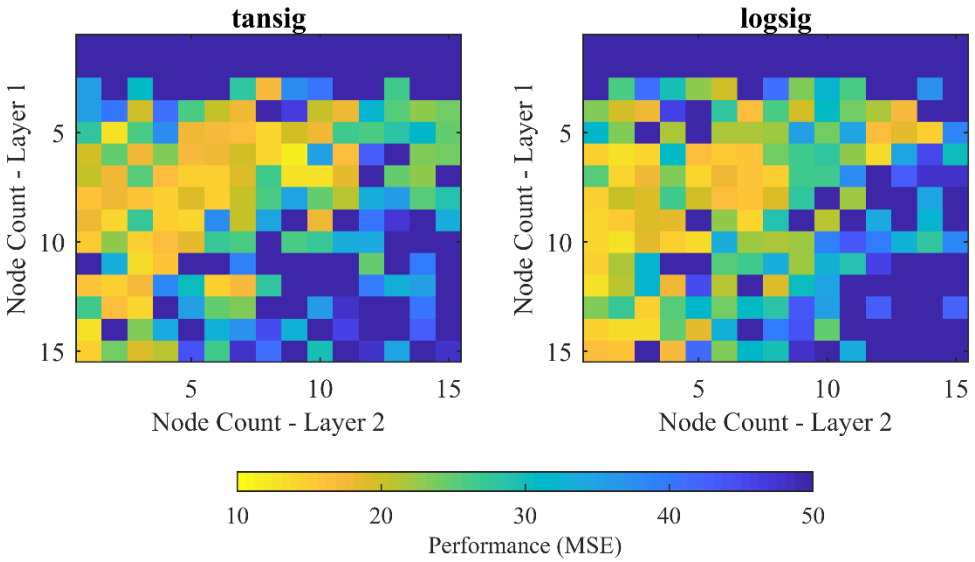

Figure 14 – Neural Network Performance by Node Combination for tansig (left) and logsig (right)

that averaging the results from many grid searches would reduce the apparent noise in the results but would require a large amount of computing time. The top performing networks (i.e., combination of hidden layer node counts and activation function) were examined for Sensor 1's model. The results of Sensor 1's best five performing networks for each activation function were briefly compared. Although all of the examined networks performed similarly, the network with the lowest test error and number of weights (recall Bayesian regularization minimizes weights to prevent overfitting) was selected.

Additionally, to reduce computing time, the neural networks for the remaining sensors' models were trained only using the tansig activation function as the network selected for Sensor 1's model used this activation function. The network with the lowest test error and number of weights from was selected for the other sensors' models. The hidden layer node combinations for each sensor's radiometric calibration model are shown in Table 4.

Table 4 – Selected Network Hidden Layer Node Counts

Sensor	**Nodes – Layer 1**	**Nodes – Layer 2**
S1	8	3
S2	14	1
S3	7	4
S4	7	4
S2, S3, & S4	6	3

4. Results & Discussion

The result analyses are limited to measurements collected between 1 and 14 meters in range. The one-meter lower bound was chosen to be near, but not at, the sensor's minimum distance of 0.5 meters in order to ensure valid measurements. Although the sensor's maximum distance under optimal conditions is 60 meters, an internal adjustment in the sensor's measurement method that occurs beyond 14 meters produces a distinct change in the accuracy and precision of the distance measurements. This change is illustrated in Figure 15 and reflected in the sensor specifications (see Table 1 in Section 3.1). Since the maximum range attainable in laboratory conditions was limited to 18 meters in this work,

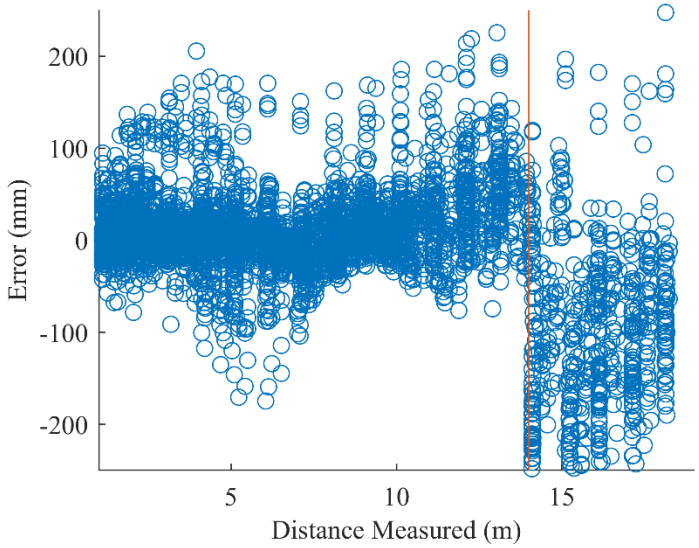

Figure 15 - Error vs Distance for All Sensors

there was insufficient data beyond the 14-meter threshold to generate radiometric calibration models capable of accommodating the abrupt change in sensor performance at 14 meters range. Therefore, the 14-meter threshold was chosen as the upper bound for all analyses.

4.1. Cross-Sensor Measurement Consistency

Comparison of the measurements reported by the four Evo 60m sensors provides insight into the consistency of the manufacturing and factory calibration processes, which, in turn, informs the suitability of using a single radiometric calibration model for all four sensors. Measurements from each Evo 60m, collected in rapid sequence (recall that the sensors interfere when operated simultaneously) were used for comparison. As noted previously, the Evo 60m reports four measurements: distance, ambient light, amplitude, and integration time. Since integration time is directly correlated with the reported amplitude, it is not compared here. Furthermore, due to the discontinuities in amplitude caused by changes in integration time, only amplitude measurements having the same integration time were compared.

Beginning with distance, visual comparison of the distance measurements between the four sensors, given in Figure 16, indicates strong agreement. However, paired t-tests of the six sensor combinations indicate only one sensor combination produces distance

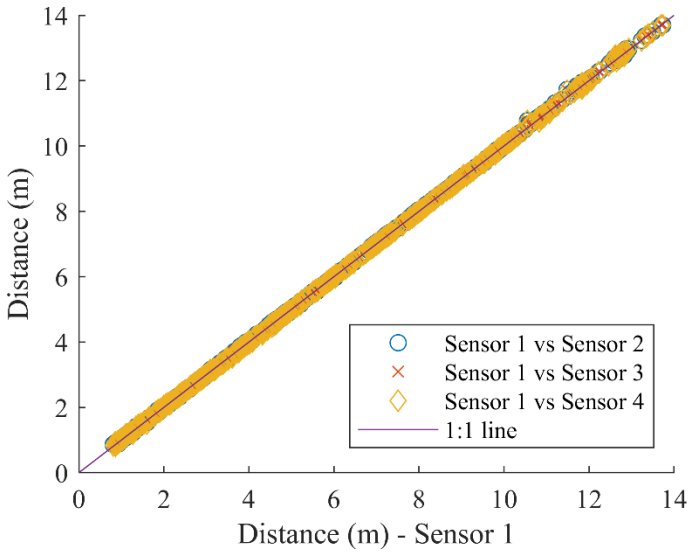

Figure 16 – Distance Comparison

measurements not statistically different at 2-sigma (95%) confidence – the Sensor 1 and Sensor 4 combination. The paired t-tests were applied to the mean setup distances (recall that a setup is comprised of 50 measurements collected at a unique distance, target, and ambient light combination) collected in controlled ambient light conditions (indoors).

The mean differences in distance for the remaining, statistically different sensor combinations ranged from 4 millimeter to 17 millimeter (see Table 5), indicating systematic biases between the sensor pairs up to three times the reported 5mm range resolution of the Evo 60m (see Table 1 in Section 3.1).

Table 5 – Mean Distance, Ambient Light, and Amplitude Differences of Each Sensor Combination

	S1-S2	S1-S3	S1-S4	S2-S3	S2-S4	S3-S4
Distance (mm)	-12.6	-16.6	0.0*	-4.0	12.6	16.6
Ambient Light (dn)	-10.1	16.1	-44.5	26.2	-34.5	-60.6
Amplitude (dn)	-45.3	-39.4	-31.2	5.9	14.0	8.1

* not statistically different

Although the ambient light and amplitude measurements reported by the four sensors have similar trends, see Figure 17, differences are more apparent. Paired t-tests confirm the ambient light measurements for all sensor combinations are statistically different at 2-sigma. Noting again that the amplitude data being compared was restricted to measurements of equal integration time, paired t-tests show all four sensors have statistically different amplitude measurements. However, the large deviation between Sensor 1's amplitude measurements and those of Sensors 2-4, readily apparent in Figure 17, is likely due to slight differences in the production processes between the purchase Sensor 1 and Sensors 2-4, as the latter group of sensors were purchased a year later than Sensor 1. Mean differences in ambient light and amplitude measurements for all sensor

combinations are given in Table 5.

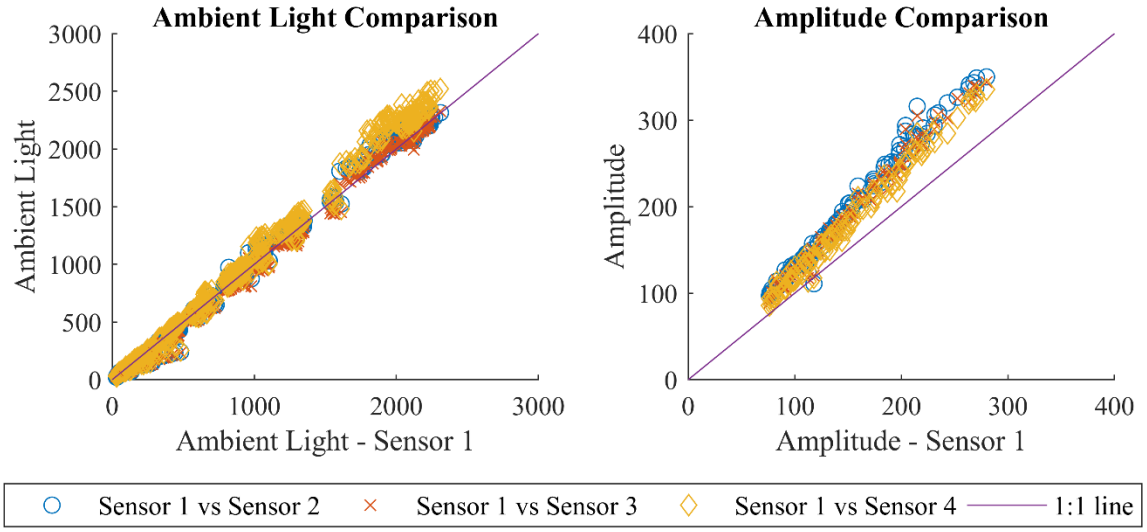

Figure 17 – Sensor Measurement Comparison of Ambient Light (left) and Amplitude (right)

Given that a neural network can be viewed as a functional approximation that relates input and output values, it is unlikely that a radiometric calibration model based on a neural network will be capable of ingesting input measurement data from all four sensors and produce equivalent levels of accuracy and precision in predicted reflectance values. However, the relatively small differences between the amplitude measurements reported by Sensors 2-4 suggest that a single radiometric calibration model for these three sensors may provide results with only a small degradation in accuracy and precision.

4.2. Radiometric Calibration

4.2.1. Performance

A performance summary is provided in Table 6 for each sensor's trained radiometric calibration model where the reflectance values predicted by the calibration models are compared to those measured with a spectroradiometer. The accuracies of the radiometric calibration models are quantified by the mean difference in reflectance (Δ) and the root

mean square error (RMSE). Both accuracy measures were computed from predicted reflectance values generated from measurements to targets spanning all range and ambient light conditions. Note that RMSE is a more robust measure of the accuracy than the mean difference in this case since it does not allow positive and negative errors in the predicted reflectance (that may exist at different ranges and ambient light conditions) to cancel one

Table 6 – Neural Network Performances for Each Sensors Trained Model

	Material	Black Foam	Gray Stucco Wall*	Gray Tabletop	Gray Painted Wall*	Red Brick*	Brown Paper	White Poster board	Plywood	Silver Door*	Brown Door*	White Painted Wall	Corkboard
	Observed Reflectance (%)	5	19	36	45	46	59	84	87	54	56	82	86
Sensor 1	Mean Reflectance	5	21	32	49	47	64	84	84	83	64	134	70
	Δ	**0**[X]	2	-4	4	**1**[X]	5	**0**[X]	-3	29	8	52	-16
	RMSE	3	3	4	5	5	6	4	4	33	12	53	16
	σ	2.7	1.8	2.2	3.2	5.2	2.9	4	2.8	15.5	9.4	8.8	2.1
Sensor 2	Mean Reflectance	4	22	31	49	46	62	82	84	82	72	138	69
	Δ	-1	3	-5	4	**0**[X]	3	-2	-3	28	16	56	-17
	RMSE	2	3	5	5	4	4	5	4	32	23	57	17
	σ	1	1.5	1.6	3	4.4	2.5	4.4	2.7	15.9	17	10.4	2.9
Sensor 3	Mean Reflectance	3	22	32	49	48	64	85	84	96	59	138	70
	Δ	-2	3	-4	4	2	5	**1**[X]	-3	42	3	56	-16
	RMSE	2	3	4	4	3	6	4	4	119	6	57	16
	σ	0.6	1.8	1.3	2.3	2.6	3.3	4.4	2.4	111	5	10.2	2.2
Sensor 4	Mean Reflectance	4	22	32	49	47	63	83	85	89	70	132	70
	Δ	-1	3	-4	4	1	4	-1	-2	35	14	50	-16
	RMSE	2	4	5	5	4	5	5	4	39	24	51	16
	σ	1.7	2.3	2.1	3.8	3.3	3	4.7	3.3	18.3	19	9	3.5

* Material Collected Outdoor, [X] No Statistical Difference at 2σ

another out. The precision of the predicted reflectance values is quantified with standard deviation (σ).

With exception of three targets suspected of specular scattering (examined in the next section) and the Corkboard material (i.e., all those targets to the right of the vertical double rule in Table 6), each calibrated sensor model predicted the test target reflectance values with mean differences of no more than 5% and RMSEs of no more than 6%. The predicted reflectance values for these well-performing targets are consistent throughout a span of different range and ambient light conditions. This is illustrated for the gray painted wall and red brick surface in Figure 18 for Sensor 1 (graphs of the remaining targets for this sensor are given in the Appendix, all other sensors performed similarly).

Except for the Corkboard target, those materials with poor reflectance predictions (greater than 5% Δ and 6% RMSE) suffered from inconsistent results, i.e., lower precision, that varied with both range and ambient light. This is evidenced by their larger standard deviations (greater than ±8%, see Table 6) and by visual comparison, e.g. see the graph for the White Wall target in Figure 18. These materials also exhibit a high positive mean difference, which is believed to be caused by specular reflection. The Corkboard target, however, is anomalous. It exhibits a low standard deviation but suffers from a large negative mean difference, shown in Figure 18. The scattering characteristics of several of the materials suspected of specular reflectance and the Corkboard are examined in the following section.

In terms of statistical significance, for almost all comparisons – 43 out of 48 – the difference between the mean predicted reflectance and the observed reflectance is statistically significant at 2-sigma according to t-tests. This is not surprising as reflectance

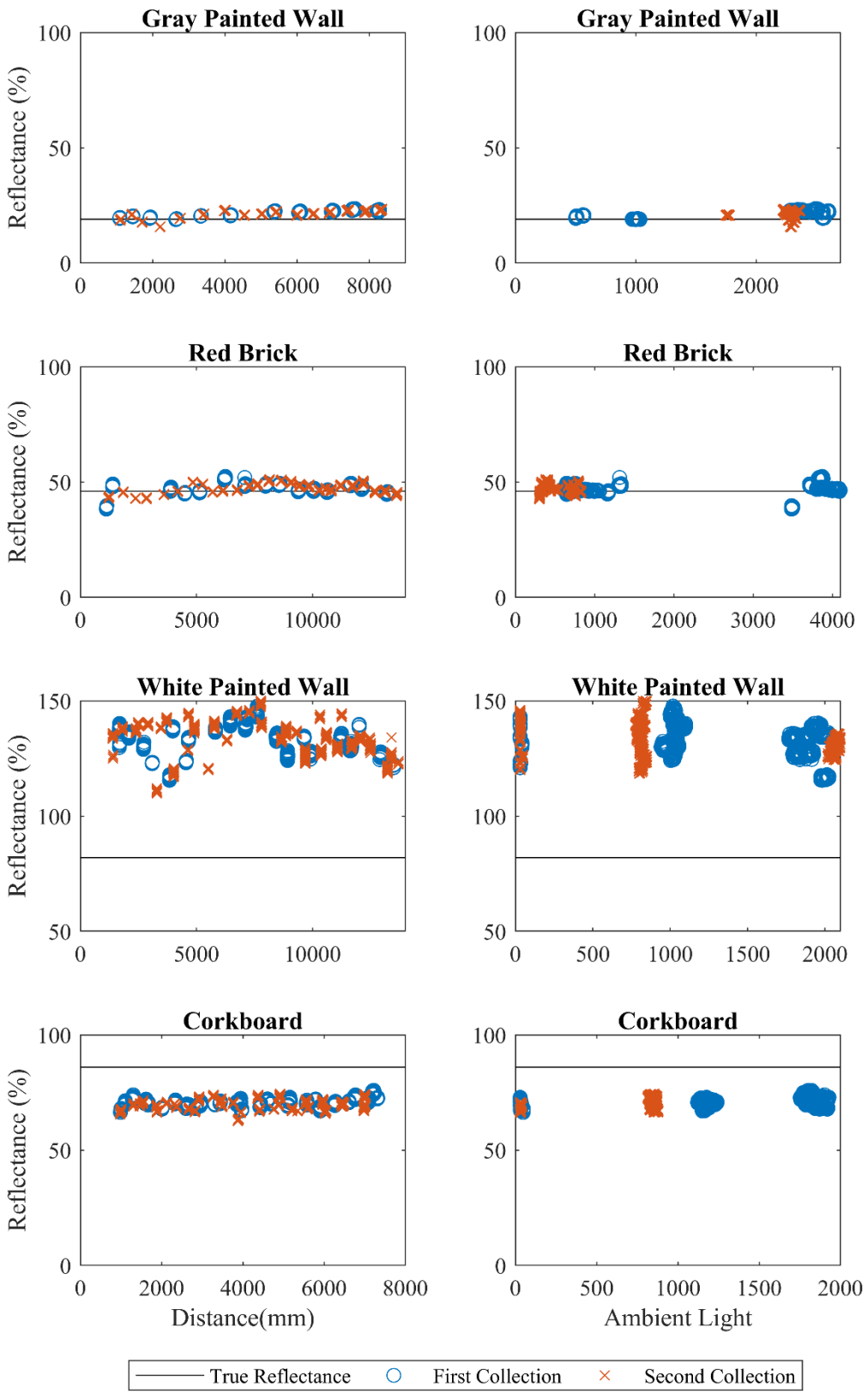

Figure 18 – Distance vs Reflectance (left), Ambient Light vs Reflectance (right) for (top to bottom): Gray Painted Wall, Red Brick, and White Painted Wall

estimates generated from lidar measurements are rarely in exact conformance with passive spectroradiometer measurements e.g. see (Hartzell, Glennie, and Finnegan 2015; Kaasalainen et al., 2011). This is caused, in part, by the different viewing geometry of active lidar sensors from typical passive sensors. Lidar sensors observe targets at the same geometry at which they are illuminated, while passive sensors typically view target surfaces at a different angle than the direction of illumination. This causes differences in phenomena such as shadow hiding and coherent backscatter, both of which influence the amount of optical power received by the sensor (Hapke et al., 1996).

Finally, it is noted that the calibration models were able to reasonably predict reflectance values of two materials with observed reflectance values outside of the bounds of the calibration data (the Plywood and White Poster Board targets), with mean differences 3% or less and RMSEs 5% or less, and standard deviations under ±5% This indicates the calibration model is capable of extrapolating beyond the bounds of the training data.

4.2.2. Effect of Incidence Angle

Several targets – Brown Door, Silver Door, and White Painted Wall – were suspected of specular reflectance based on their performance results reviewed in the prior section. This hypothesis was qualitatively investigated by comparing reflectance values produced from observations of two of these targets, the Silver Door and White Painted Wall, at multiple incidence angles to the reflectance values predicted by Equation (11), where it is shown that the amount of light reflected by a Lambertian (non-specular) target is proportional to the cosine of the incidence angle. Two of the OSB calibration panels, the 62% and 50% reflectance targets, were also examined. Graphs of the reflectance values

predicted by the calibration models versus those predicted by the cosine relationship (cosine of the incidence angle multiplied by the target's observed reflectance value at normal incidence) are given in Figure 19.

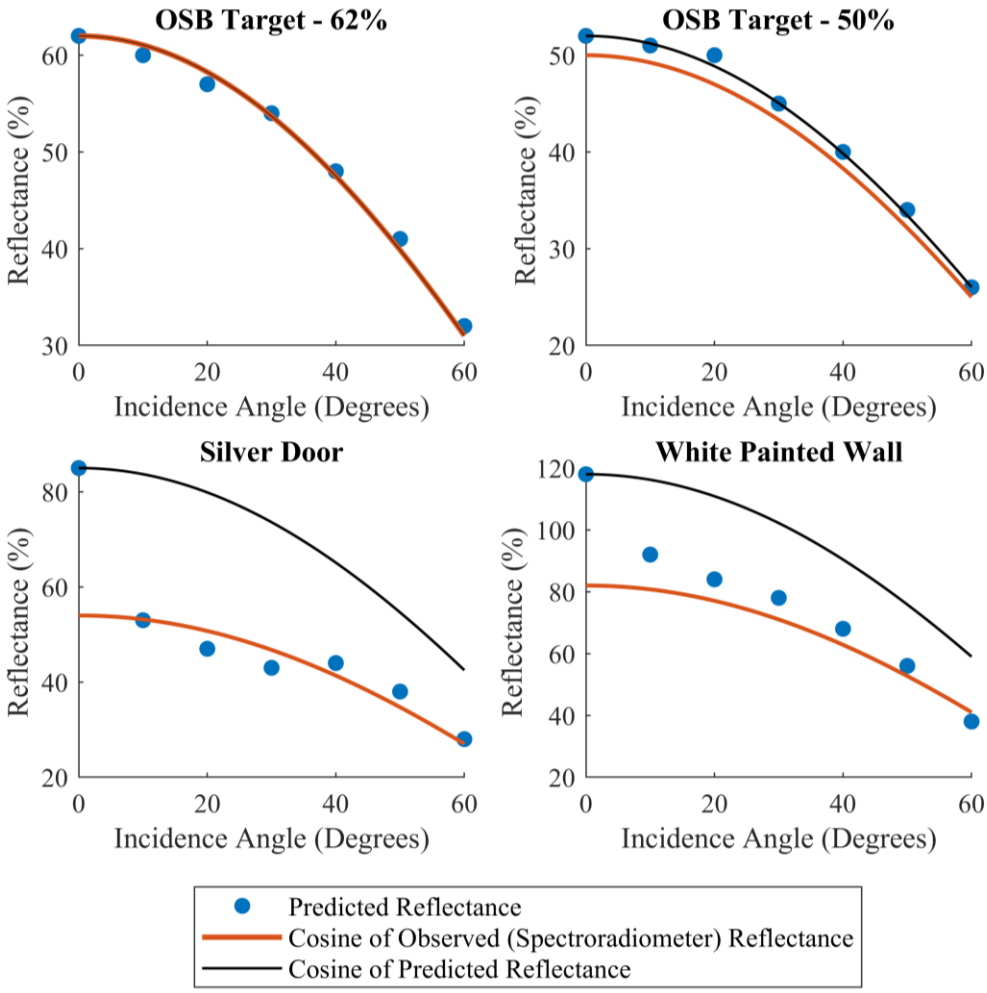

Figure 19 – Scattering Characteristics for (top to bottom, left to right): OSB Target 2, OSB Target 3, Silver Door, and White Painted Wall.

The calibration targets (top two graphs of Figure 19) follow the trend predicted by Equation (12), whereas the targets suspected of specular reflection exhibit a strong peak at 0-degree incidence (bottom two graphs of Figure 19), indicating the presence of specular, or mirror-like, scattering at near-normal observation geometries. These specular targets also exhibit much more variation in their predicted reflectance values than the OSB panels,

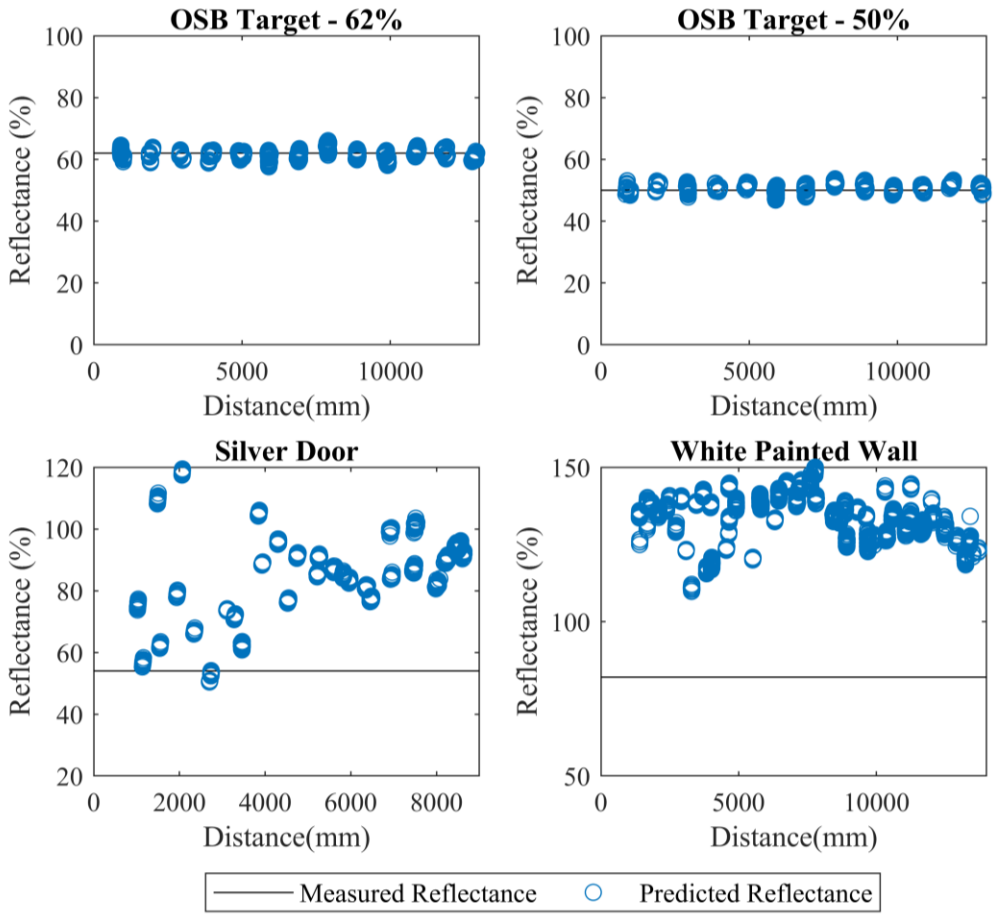

Figure 20 – Predicted Reflectance for (top to bottom, left to right): OSB Target 2, OSB Target 3, Silver Door, and Brown Door.

which is illustrated in Figure 20 and evidenced by their relatively large standard deviations (see Table 6). The large standard deviations are believed to result from small variations in the target incidence angle between the sensor setups due to minor inconsistencies in the sensor alignment with respect to the targets as well as non-planar characteristics of some of the targets (e.g. the corrugated geometry of the Silver Door target). It is noted that the Brown Door target also likely suffers from specular reflection based on its relatively high standard deviation and mean difference values. Similar analysis was performed for the corkboard target, which was found to exhibit Lambertian scattering characteristics. Unfortunately, this does not provide any potential reasons for the very low reflectance

predicted by the calibration models for the Corkboard target.

4.2.3. Temporal Stability

For a calibration model to produce consistent results over time, the measurements fed into the model must also be consistent over time. Therefore, the test targets were observed twice, separated by at least a month in time, and the mean predicted reflectance for each setup (recall that a setup is a group of measurements collected at a unique combination of target type, distance, and ambient light level) compared between collection dates. Visual comparison for Sensor 1 is illustrated in Figure 21, where the non-specular target mean

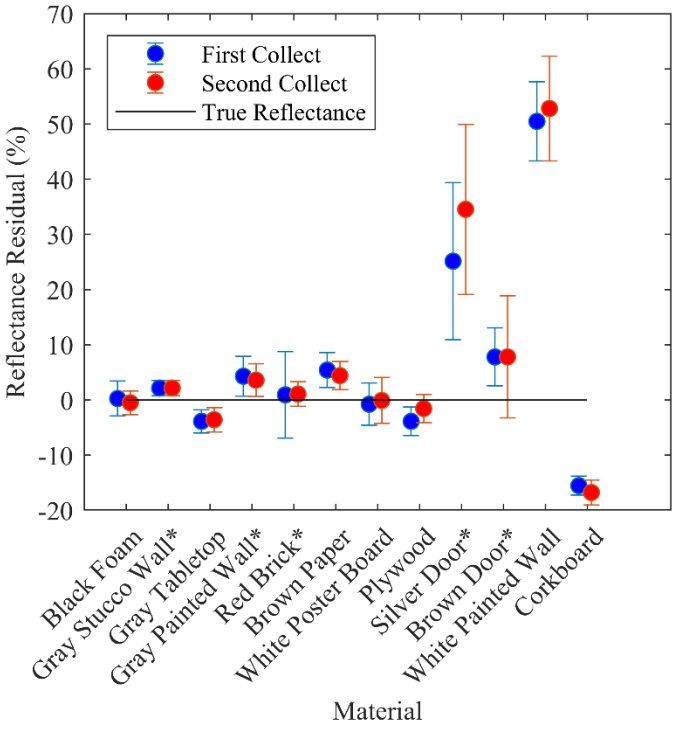

Figure 21 – Temporal Variation by Material for Sensor 1 with 1-sigma Error Bars
* Material Collected Outdoors

reflectance values appear to align, and the error bars indicate a high degree of agreement within the bounds of the measurement precision. The results are similar for Sensors 2-4 and are given in the Appendix.

The visual interpretation of temporal agreement is supported by two sample t-tests of the mean reflectance values from the temporally separated collections, which found that 45 of 48 comparisons (4 sensors ×12 materials = 48) were not statistically different at 2-sigma confidence. Table 7 shows the difference between the mean reflectance of each temporal collection. For the three pairs tested to be statistically different, only one of those was a non-specular target with a difference between mean reflectance values of 2.3%. This suggests that while the temporal differences may be statistically significant in some cases, they are likely not practically significant, particularly for a low-cost remote sensing instrument.

Table 7 – Difference in Mean Reflectance for Temporally Separated Collections

	Black Foam	Gray Stucco Wall*	Gray Tabletop	Gray Painted Wall*	Red Brick*	Brown Paper	White Poster board	Plywood	Silver Door*	Brown Door*	White Painted Wall	Corkboard
Sensor 1	0.8	0.4	-0.3	0.7	-0.1	1	-0.7	**-2.3^{X}**	-9.4	0	-2.3	**1.2^{X}**
Sensor 2	0.7	-0.5	-0.7	0.6	-0.6	0.1	0.4	-1.6	-8.1	2.3	-1.3	1.4
Sensor 3	0.3	0.3	-0.6	0.4	0	0.5	-0.2	-1.4	-7	1.3	-2	0.6
Sensor 4	0.4	-1	-0.8	0.4	0.2	-0.2	0.4	-1.5	**-12.4^{X}**	1	-2.3	0.2

* Material Collected Outdoors ^{X} Statistically Significant at 2σ

4.2.4. Calibration Model Multi-Sensor Performance

If a single model can provide equivalent reflectance predictions for multiple sensors, individual calibrations for each sensor may not be necessary. This is attractive in terms of efficiency if many sensors are to be calibrated. Results produced by cross-application of each of the four sensor-specific calibration models to the test target data collected by all four sensors were therefore compared. For clarity, the specular targets and Corkboard were

not included in the analysis. The best performance, quantified by RMSE in Table 8, is achieved when applying the sensor-specific models to their own test target observations.

Table 8 – RMSE of the Eight Well Performing Test Materials for Each Sensor and Each Model

		Model				
		S1	S2	S3	S4	S2, S3, & S4
Data	Sensor 1	4	13	10	9	10
	Sensor 2	18	4	6	7	5
	Sensor 3	15	5	4	5	5
	Sensor 4	12	6	4	4	5

The performance of the cross-application of the sensor-specific calibration models follows the patterns reported in Section 4.1, where the consistency of the reported measurements was compared between the four sensors: cross-application of the sensor-specific calibration models perform better for Sensors 2-4 and worst when applying Sensor 1's calibration model to the test target data collected by Sensors 2-4 and vice-versa. Note that these results are 'global' – all RMSE values encompass all eight of the well-performing test targets. Similar results are found when examining the test target materials individually. In addition to the RMSE analysis, mean reflectance values for the 12 targets produced from an example cross-application are graphed in Figure 22 to provide additional context to the cross-application performance.

Finally, in addition to the self and cross-application of the individual sensor calibration models, a single calibration model was trained using data from Sensors 2-4 and applied to the test target data collected by those sensors. The results (see Table 6) are reasonable, with performance being slightly worse than self-application of the sensor-specific models but better than the cross-applications.

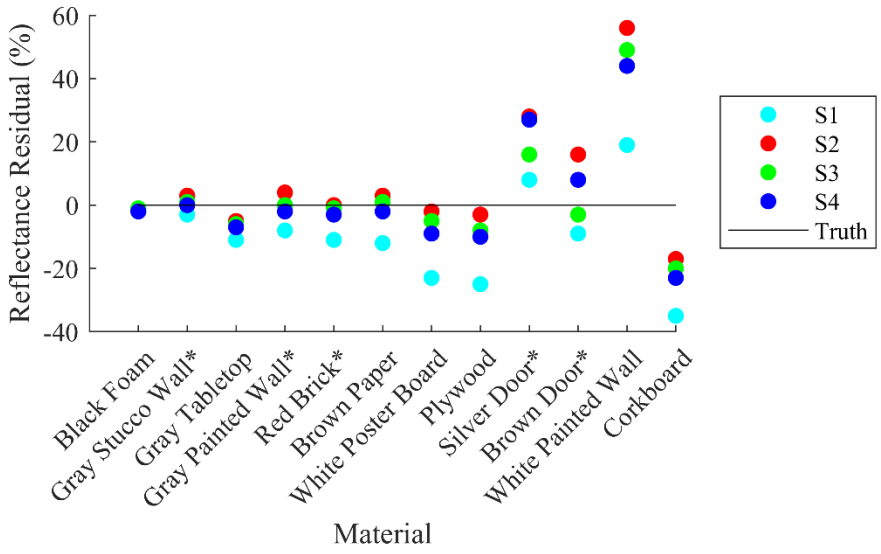

Figure 22 – Performance of Each Sensor's Data Using the Model Trained with Sensor 2 Data

4.3. Geometric Calibration

The accuracy and precision of the Evo 60m range measurements are examined in this section. As noted previously, the analysis is limited to a maximum of 14 meters in range due to the sensor's internal measurement adjustment at this distance and limitations in lab space. It is also noted that the manufacturer supplies an accuracy specification, but not a precision specification, to which the results can be compared.

4.3.1. Precision

Table 9 shows the Evo 60m range precision (standard deviation) of all four sensors for all materials, ranges, and ambient light conditions. The computed precisions are all under ±10 millimeters, which is well under the stated *accuracy* of ±40 millimeters (no precision value is supplied). However, this single number fails to show the effects that different variables, such as signal return power and ambient light, have on the Evo 60m's precision.

As mentioned in Section 2.3, (Wujanz et al., 2017) proposed a power law relating the

Table 9 – Geometric Precision

Sensor	Precision (mm)
Sensor 1	9.4
Sensor 2	9.5
Sensor 3	8.6
Sensor 4	9.0

precision of lidar range measurements to the return signal intensity. The use of a power law relationship with respect to lidar signal return power agrees with standard models for predicting ranging variance for time-of-flight and continuous wave lidar (see (Baltsavias 1999)). Per Equation (11), a power law is also an appropriate model for ITOF ranging variance. Assuming a constant ambient light level, Equation (11) predicts that ITOF range variance is proportional to the inverse square root of the measured ITOF amplitudes. Note that although the amplitude reported by the Evo 60m is a measure of signal intensity, it varies with the sensor integration time and, therefore, is not appropriate for comparison to the range precision. Instead, a proxy for return signal power is formed by normalizing the predicted target reflectance values by the square of the measured range to produce a quantity proportional to the received optical power per Equation (11). A graph of the relationship between observed range precision and normalized reflectance for all setups measured with all four sensors is shown in Figure 23. A power law relationship is fit to the data and indicates a similar trend, albeit with a higher floor in precision (at high return powers) than the model can accommodate. The high floor is a result of the Evo 60m's range quantization of five millimeters.

The precision of the Evo 60m's range measurements also decreases with the increased ambient light, i.e., with lower signal to noise ratios. This effect can be seen in Figure 23

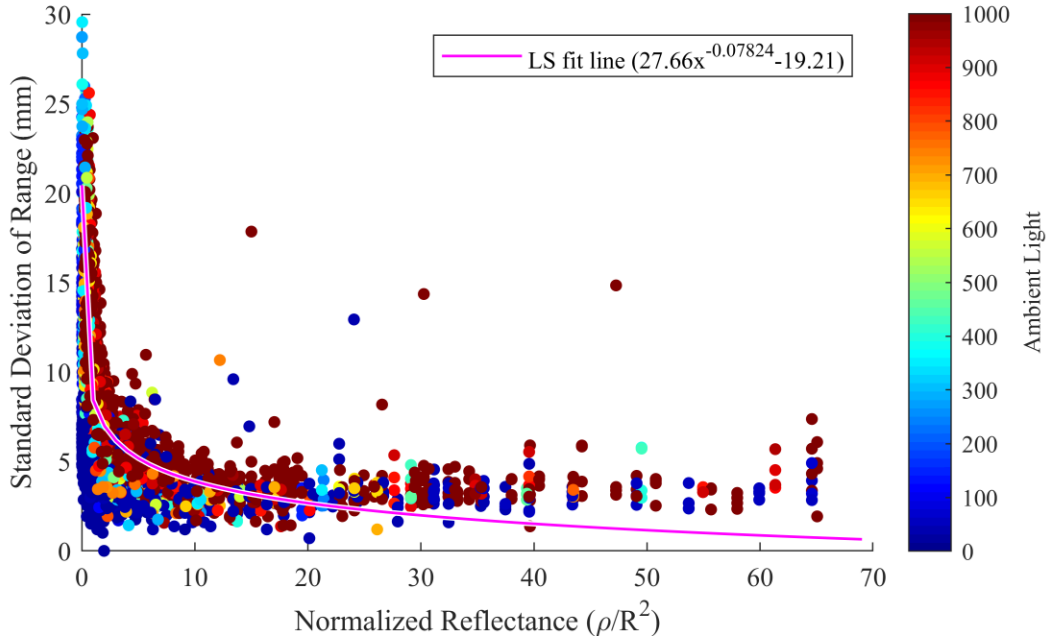

Figure 23 – Standard Deviation of Distance Measurements for All OSB Target and Test Materials from all Sensors at Normalized Reflectance

where the data points are colored by ambient light level, and is also highlighted in Figure 24, where the range precision for a single sensor and single target (Sensor 1, 80% reflectance OSB target) is graphed versus the measured range and colored by ambient light

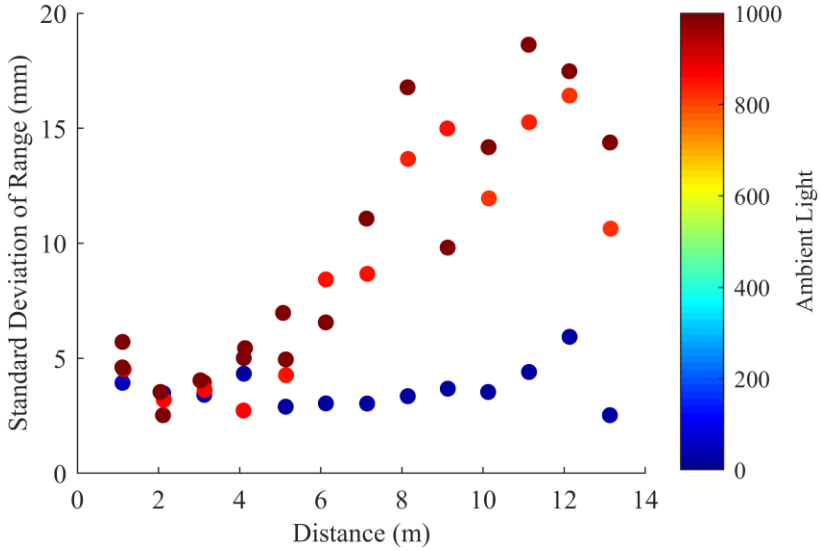

Figure 24 – Calibration OSB 80%

level. As range increases, and return power decreases, the negative impact of higher ambient light levels on ranging precision is clearly seen.

4.3.2. Accuracy

Whereas precision is concerned with the repeatability of the range measurements, accuracy considers the presence or absence of systematic errors that bias the range

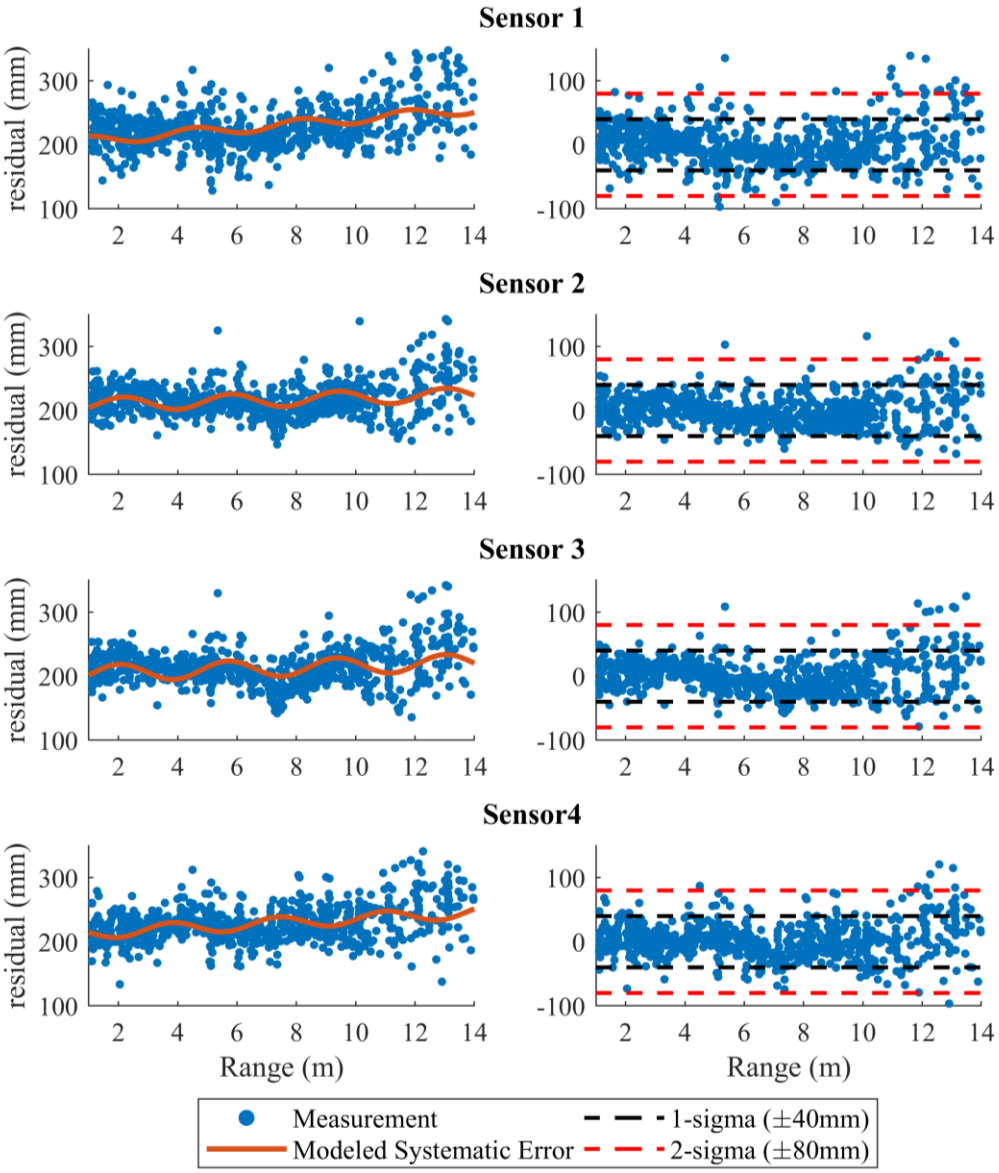

Figure 25 – Residual Before (left) and After (right) Removal of Modeled Systematic Error. Dashed black and red lines are the manufacturer's stated accuracy at 1 and 2-sigma.

measurements from the true values. Range residuals, defined as the difference between the ranges measured by the Leica Disto and the Evo 60m sensors, for targets with reflectance values greater than 20% were therefore examined for the presence of systematic errors. Ranges from low reflectance targets (<20%) were not considered to avoid spurious results due to their low ranging precision. Range residuals versus target range are plotted for the four sensors in Figure 25. An offset of approximately 200 millimeters is clearly evident and, to a lesser extent, a cyclical component with a period of 3-4 meters in range can be seen in the graphs for the four sensors. Note that the large offset is due to the physical distance between the Leica Disto and Evo 60m sensor origins. This offset could not be removed prior to this analysis because the location of the ranging origin for Evo 60m sensors is unknown. To date, this information is not found on any available specification sheets and several inquiries with Terabee have gone unanswered.

In addition to the offset and apparent periodic component, the plots for Sensors 1 and 4 in Figure 25 suggest that residuals may also increase as a function of range, i.e., the measured Evo 60m ranges may also be subject to a scale factor. A residual error model incorporating an offset, a scale factor, and a periodic component can be expressed as,

$$a_0 + a_1 x + a_2 \sin\left(\frac{2\pi}{a_3} + a_4\right), \tag{18}$$

where a_0 is the offset, a_1 is the scale factor, and a_2, a_3, a_4 are the amplitude, period, and phase shift of the periodic component. A least squares fit of the error model to the residuals was solved for each sensor. The resulting solved parameters, shown in Table 10, were all found to be statistically different from zero at 95% confidence.

Only Sensors 2 and 3 share a statistically consistent model (i.e., none of the parameters are statistically different). All other sensor combinations have at least two parameters that

Table 10 – Solved Systematic Error Model Parameters

	Offset (mm)	**Scale**	**Amplitude (mm)**	**Period (m)**	**Shift (m)**
Sensor 1	202.2 (±5.1)	3.8 (±0.7)	-7.5 (±3.2)	3.8 (±0.3)	3.1 (±1.0)
Sensor 2	207.5 (±3.6)	1.3 (±0.5)	-10.9 (±2.3)	3.6 (±0.1)	1.0 (±0.4)
Sensor 3	202.6 (±3.8)	1.4 (±0.5)	-13.2 (±2.6)	3.7 (±0.1)	1.2 (±0.4)
Sensor 4	210.9 (±3.9)	2.5 (±0.5)	-9.4 (±2.5)	4.1 (±0.2)	-1.9 (±0.5)

are statistically different. Examining the 95% confidence intervals of the individual model parameters across all four sensors, only the amplitude of the periodic component is statistically equivalent across all sensors (see Table 11). Scale and phase shift are only statistically equivalent between sensors 2 and 3. These results indicate that although a common model may be appropriate for calibrating the sensor ranges, the best results are obtained from unique calibrations, i.e., the error model parameters should not be shared between sensors.

Table 11 – Statistical Significance at 95% Confidence of the Solved Systematic Error Model for Sensor Pair

	S1-S2	S1-S3	S1-S4	S2-S3	S2-S4	S3-S4
Offset	Same	Same	Same	Same	Same	Different
Scale	Different	Different	Different	Same	Different	Different
Amplitude	Same	Same	Same	Same	Same	Same
Period	Same	Same	Same	Same	Different	Different
Shift	Different	Different	Different	Same	Different	Different

Although the spread of the solved offset values is approximately 8 millimeters, the mean offset value indicates the physical location of the Evo 60m's range reference point is located approximately in the middle of the sensor. This is illustrated in Figure 25. If the solved offset values are removed from the range residuals, RMSEs generated from the resultant residuals (see Table 12) fall below the manufacturer's stated accuracy level of ±40 millimeters for Sensors 2-4. Sensor 1's RMSE lies just above the ±40 millimeter

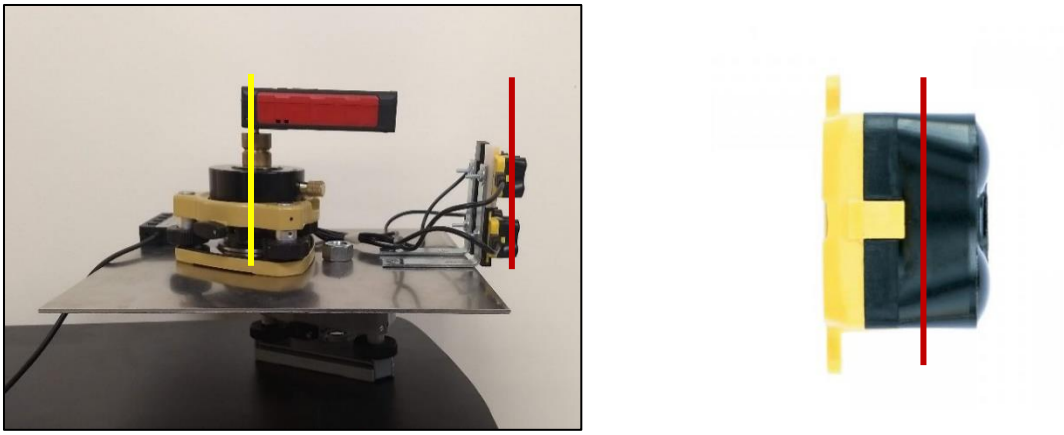

Figure 26 – EDM Reference Point (yellow line) and Determined Evo 60m Range Reference Point (red line)

threshold at ±43 millimeters. This indicates that given knowledge of the sensor origin point, the ranging accuracy of the Evo 60m largely falls within the manufacturer's stated accuracy specification. Although not likely to be applied in a practical setting, the RMSEs are improved (decreased) by 12%-25% when applying the entire systematic error model instead of only the offset (see Table 12).

Table 12 – Root Mean Squared Error with and without Systematic Error

Sensor	No Systematic Error Removal	Only Offset Removed	Entire Systematic Error Removed
S1	230.2	43.7	32.9
S2	219.3	27.2	23.9
S3	216.0	30.1	26.1
S4	229.3	32.3	26.9

All measurements are (±mm)

5. Conclusions

Radiometric calibration of traditional lidar sensors that employ direct time of flight or phase-based ranging methods is well established. However, emerging low-cost, short-range lidar sensors utilize different ranging methods, and, consequently, report measurements not appropriate for use in existing radiometric calibration techniques. This work examined an LED-based lidar sensor, the Terabee Evo 60m, which determines target ranges through indirect time of flight. A unique characteristic of this sensor is that the reported signal amplitudes are not smoothly proportional to incident optical power but instead exhibits large discontinuities as the sensor automatically adjusts the amount of time required to make a range measurement in response to changing signal and noise levels.

An empirical radiometric calibration model based on a neural network was proposed as an alternative to existing calibration techniques for the Evo 60m lidar sensor. The network ingests the four measurements reported by the Evo 60m—range, amplitude, integration time, and ambient light—and outputs an estimate of target reflectance. For non-specular materials, the network model predicts target reflectance values consistent with spectroradiometer measurements to within ±6% RMSE (accuracy) or better with precisions of ±5% or less. This performance is consistent with that of traditional lidar sensors and was able to be attained with four different Evo 60m sensors. The measurements reported by the four sensors were found to be most similar to one another for those sensors purchased at the same time (three sensors were purchased a year later than the first sensor), but largely different when statistically tested at 95% confidence. Accordingly, each sensor performs best when using a radiometric calibration model trained on its own measurements, i.e., reflectance prediction performance is degraded when using a network trained on data

collected from one or more of the other sensors.

In addition to the radiometric analysis, the ranging performance of the Evo 60m was examined. On average, range precision was found to be less than ±10 millimeters for all targets in all conditions. Range precision approached the sensor quantization value of ±5 millimeters for targets with relatively high signal return power, but rapidly increased at low signal return power levels. The relationship between signal return power and range precision approximately followed a power law, similar to traditional time of flight and continuous wave lidar sensors. In terms of accuracy, when the physical offset between the Evo 60m and Leica Disto ranges was modeled and removed, the ranging accuracy was found to be in conformance with the manufacturer's stated specification of ±40 millimeters for three out of the four sensors tested. Although further improvements in ranging accuracy were able to be achieved by modeling and removing systematic scale and periodic error components, these are likely not of practical concern for such an inexpensive sensor.

The work in this thesis was originally inspired by the desire for a low-cost multispectral lidar sensor. The performance of the proposed radiometric calibration model is in line with current techniques, and thus applicable to future research with multiple wavelength LED-based lidar sensors. Furthermore, the neural network based calibration model represents a generic approach that may be applicable to other low-cost lidar sensors, which may be an avenue for future research. Ultimately, the neural network required to build a radiometric calibration model is simple and quite small. Embedding such a network into sensor firmware may be of interest to manufacturers in the future to provide additional and valuable information about target radiometry to end users.

References

Baltsavias, E.P. 1999. “Airborne Laser Scanning: Basic Relations and Formulas.” *ISPRS Journal of Photogrammetry and Remote Sensing* 54 (2–3): 199–214. https://doi.org/10.1016/s0924-2716(99)00015-5.

Bellisai, S., F. Villa, S. Tisa, D. Bronzi, and F. Zappa. 2011. “Indirect Time-of-Flight 3D Ranging Based on SPADs.” *Quantum Sensing and Nanophotonic Devices IX* 8268 (January 2012): 82681C. https://doi.org/10.1117/12.908222.

Bergstrand, Erik. 1949. “Measurement of Distances by High Frequency Light Signalling.” *Bulletin Géodésique* 23 (1): 81–92. https://doi.org/10.1007/BF02520682.

Charbon, Edoardo. 2014. “Introduction to Time-of-Flight Imaging.” *Proceedings of IEEE Sensors* 2014-Decem (December): 610–13. https://doi.org/10.1109/ICSENS.2014.6985072.

Corrigan, Fintan. 2019. “12 Top Lidar Sensors for UAVs, Lidar Drones and So Many Great Uses.” DroneZon. 2019. https://www.dronezon.com/learn-about-drones-quadcopters/best-lidar-sensors-for-drones-great-uses-for-lidar-sensors/.

Dan Foresee, F., and M. T. Hagan. 1997. “Gauss-Newton Approximation to Bayesian Learning.” *IEEE International Conference on Neural Networks - Conference Proceedings* 3: 1930–35. https://doi.org/10.1109/ICNN.1997.614194.

Gavin, Henri P. 2019. “The Levenburg-Marqurdt Algorithm For Nonlinear Least Squares Curve-Fitting Problems.” *Duke University*, 1–19. http://people.duke.edu/~hpgavin/ce281/lm.pdf.

Goodfellow, Ian, Yoshua Bengio, and Aaron Courville. 2016. *Deep Learning*. MIT Press.

http://www.deeplearningbook.org.

Gordon, S., N. Davies, D. Keighley, D. Lichti, and J. Franke. 2005. “A Rigorous Rangefinder Calibration Method for Terrestrial Laser Scanners.” *Journal of Spatial Science* 50 (2): 91–96. https://doi.org/10.1080/14498596.2005.9635052.

GrindGPS. 2015. “50 Applications for Lidar.” 2015. https://grindgis.com/data/lidar-data-50-applications.

Hapke, Bruce, Dominick DiMucci, Robert Nelson, and William Smythe. 1996. “The Cause of the Hot Spot in Vegetation Canopies and Soils: Shadow-Hiding versus Coherent Backscatter.” *Remote Sensing of Environment* 58 (1): 63–68. https://doi.org/10.1016/0034-4257(95)00257-X.

Hartzell, Preston J., Craig L. Glennie, and David C. Finnegan. 2015. “Empirical Waveform Decomposition and Radiometric Calibration of a Terrestrial Full-Waveform Laser Scanner.” *IEEE Transactions on Geoscience and Remote Sensing* 53 (1): 162–72. https://doi.org/10.1109/TGRS.2014.2320134.

Hastie, Trevor, Robert Tibshirani, and Jerome Friedman. 2009. *The Elements of Statistical Learning*. Springer Series in Statistics. New York, NY: Springer New York. https://doi.org/10.1007/b94608.

Höfle, Bernhard, and Norbert Pfeifer. 2007. “Correction of Laser Scanning Intensity Data: Data and Model-Driven Approaches.” *ISPRS Journal of Photogrammetry and Remote Sensing* 62 (6): 415–33. https://doi.org/10.1016/j.isprsjprs.2007.05.008.

Jazayeri, Kian, Moein Jazayeri, and Sener Uysal. 2016. “Comparative Analysis of Levenberg-Marquardt and Bayesian Regularization Backpropagation Algorithms in

Photovoltaic Power Estimation Using Artificial Neural Network." In *Lecture Notes in Computer Science (Including Subseries Lecture Notes in Artificial Intelligence and Lecture Notes in Bioinformatics)*, 9728:80–95. https://doi.org/10.1007/978-3-319-41561-1_7.

Kaasalainen, Sanna, Antero Kukko, Tomi Lindroos, Paula Litkey, Harri Kaartinen, Juha Hyyppä, and Eero Ahokas. 2008. "Brightness Measurements and Calibration with Airborne and Terrestrial Laser Scanners." *IEEE Transactions on Geoscience and Remote Sensing* 46 (2): 528–33. https://doi.org/10.1109/TGRS.2007.911366.

Kaasalainen, Sanna, Ulla Pyysalo, Anssi Krooks, Ants Vain, Antero Kukko, Juha Hyyppä, and Mikko Kaasalainen. 2011. "Absolute Radiometric Calibration of ALS Intensity Data: Effects on Accuracy and Target Classification." *Sensors* 11 (11): 10586–602. https://doi.org/10.3390/s111110586.

Koyama, Moriaki, and Tatsuo Shiina. 2011. "Development of LED Mini-Lidar." *2011 Int. Quantum Electron. Conf., IQEC 2011 and Conf. Lasers and Electro-Optics, CLEO Pacific Rim 2011 Incorporating the Australasian Conf. Optics, Lasers and Spectroscopy and the Australian Conf.*, no. September: 544–45. https://doi.org/10.1109/IQEC-CLEO.2011.6193859.

Kriesel, David. 2007. *A Brief Introduction to Neural Networks*.

Li, Larry. 2014. "Time-of-Flight Camera–An Introduction." *Texas Instruments - Technical White Paper*, no. January: 10.

Lichti, Derek D. 2007. "Error Modelling, Calibration and Analysis of an AM-CW Terrestrial Laser Scanner System." *ISPRS Journal of Photogrammetry and Remote Sensing* 61

(5): 307–24. https://doi.org/10.1016/j.isprsjprs.2006.10.004.

Maiman, T H. 1960. “Stimulated Optical Radiation in Ruby.” *Nature* 187 (4736): 493–94. https://doi.org/10.1038/187493a0.

Melexis. 2017. “Time-of-Flight Basics,” 1–14.

Møller, Martin F. 1990. “PREPRINT A Scaled Conjugate Gradient Algorithm for Fast Supervised Learning Supervised Learning.” *Science*.

NOAA. 2007. “AGA Geodimeters, Models 4D and 4L.” 2007. https://celebrating200years.noaa.gov/distance_tools/geodimeters_4d_4l.html.

Nwankpa, Chigozie, Winifred Ijomah, Anthony Gachagan, and Stephen Marshall. 2018. “Activation Functions: Comparison of Trends in Practice and Research for Deep Learning,” November, 1–20. http://arxiv.org/abs/1811.03378.

Perenzoni, Matteo, and David Stoppa. 2011. “Figures of Merit for Indirect Time-of-Flight 3D Cameras: Definition, Experimental Evaluation.” *Remote Sensing* 3 (11): 2461–72. https://doi.org/10.3390/rs3112461.

Satterwhite, Melvin B., and C. Scott Allen. 2003. “A Novel Low-Cost Approach for Large Gray-Toned Fabric Panels for Calibrating Remotely Sensed VIS/NIR/SWIR Data.” *Algorithms and Technologies for Multispectral, Hyperspectral, and Ultraspectral Imagery IX* 5093: 163. https://doi.org/10.1117/12.488364.

Shan, Jie, and Charles K. Toth, eds. 2009. *Topographic Laser Ranging and Scanning - Principles and Processing*. CRC Press.

Taylor, Barry N, and Chris E Kuyatt. 1994. “Guidelines for Evaluating and Expressing the Uncertainty of NIST Measurement Results.” National Institute of Standards and

Technology.

Terabee. 2017. “TeraRanger Evo 60m Specification Sheet.” https://www.terabee.com/wp-content/uploads/2018/10/TeraRanger-Evo-60m-Specification-sheet.pdf.

———. 2018. “Test Results Report for TeraRanger Evo 60m Sensor Potential Maximum Range in Varying Outdoor Conditions.” *Terabee*.

Vosselman, George, and Hans-Gerd Maas, eds. 2010. *Airborne and Terrestrial Laser Scanning*. Whittles Publishing.

Wagner, Wolfgang. 2010. “Radiometric Calibration of Small-Footprint Full-Waveform Airborne Laser Scanner Measurements: Basic Physical Concepts.” *ISPRS Journal of Photogrammetry and Remote Sensing* 65 (6): 505–13. https://doi.org/10.1016/j.isprsjprs.2010.06.007.

Wagner, Wolfgang, Andreas Ullrich, Vesna Ducic, Thomas Melzer, and Nick Studnicka. 2006. “Gaussian Decomposition and Calibration of a Novel Small-Footprint Full-Waveform Digitising Airborne Laser Scanner.” *ISPRS Journal of Photogrammetry and Remote Sensing* 60 (2): 100–112. https://doi.org/10.1016/j.isprsjprs.2005.12.001.

Wandinger, Ulla. 2006. “Introduction to Lidar.” *Lidar*, 1–18. https://doi.org/10.1007/0-387-25101-4_1.

Wehr, Aloysius, and Uwe Lohr. 1999. “Airborne Laser Scanning - An Introduction and Overview.” *ISPRS Journal of Photogrammetry and Remote Sensing* 54 (2–3): 68–82. https://doi.org/10.1016/S0924-2716(99)00011-8.

Wujanz, D., M. Burger, M. Mettenleiter, and F. Neitzel. 2017. “An Intensity-Based Stochastic Model for Terrestrial Laser Scanners.” *ISPRS Journal of Photogrammetry and Remote Sensing* 125: 146–55. https://doi.org/10.1016/j.isprsjprs.2016.12.006.

Yonaba, H., F. Anctil, and V. Fortin. 2010. “Comparing Sigmoid Transfer Functions for Neural Network Multistep Ahead Streamflow Forecasting.” *Journal of Hydrologic Engineering* 15 (4): 275–83. https://doi.org/10.1061/(ASCE)HE.1943-5584.0000188.

Appendix

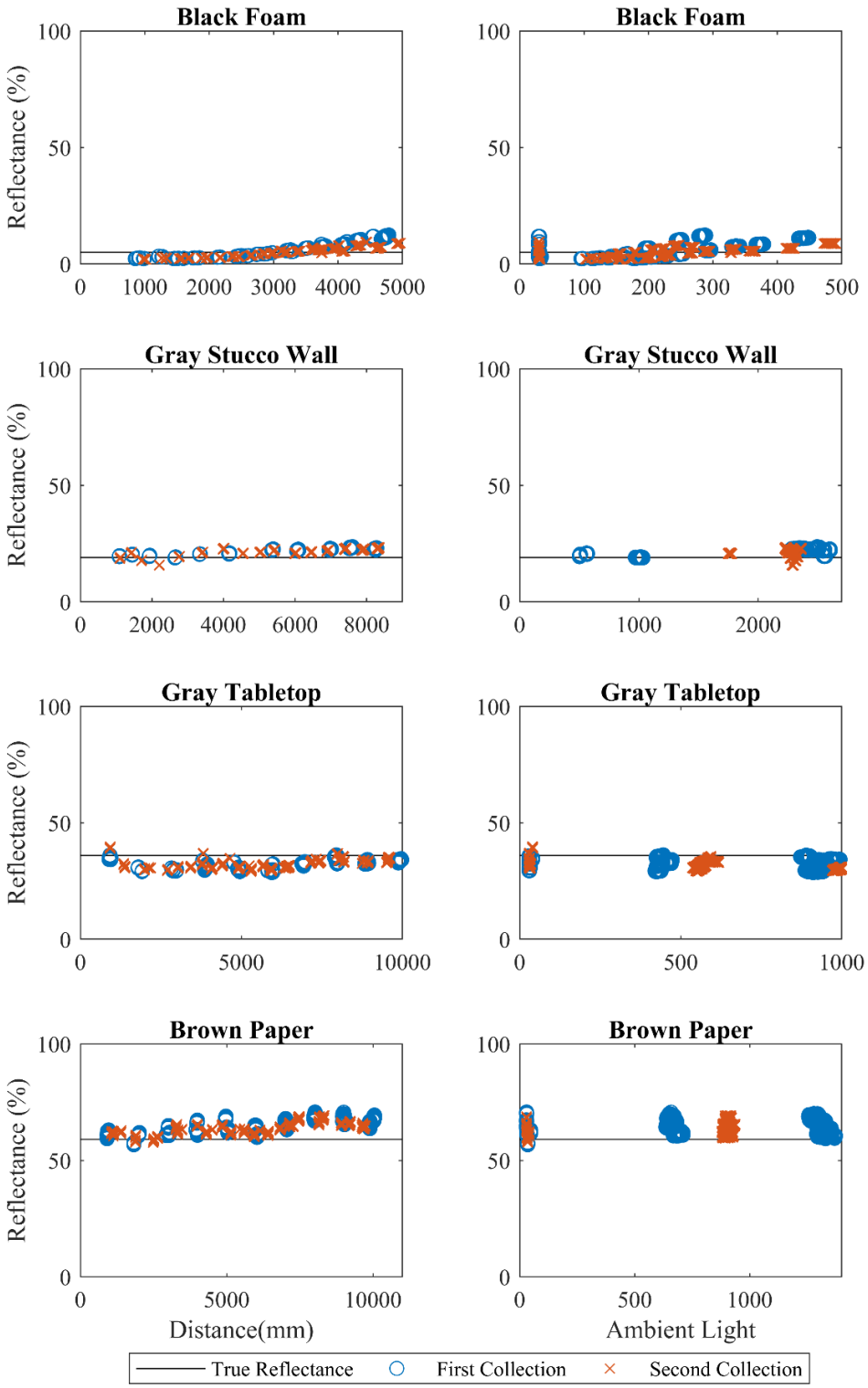

Figure 27 – Sensor 1 Performance Consistency for Black Foam, Gray Stucco Wall, Gray Tabletop, and Brown Paper (Reflectance vs Distance – Left, Reflectance vs Ambient Light – Right)

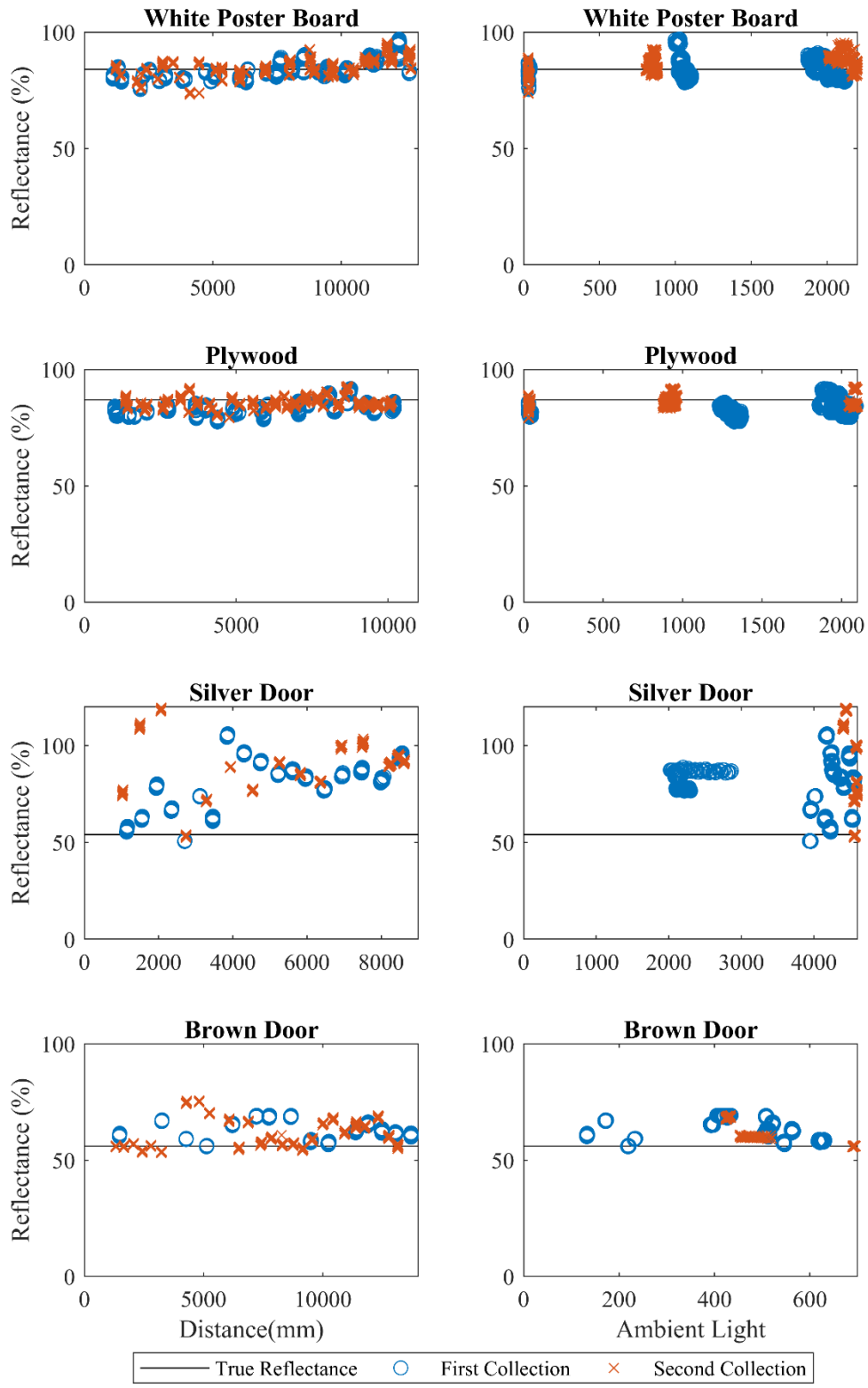

Figure 28 – Sensor 1 Performance Consistency for White Poster Board, Plywood, Silver Door, and Brown Door (Reflectance vs Distance – Left, Reflectance vs Ambient Light – Right)

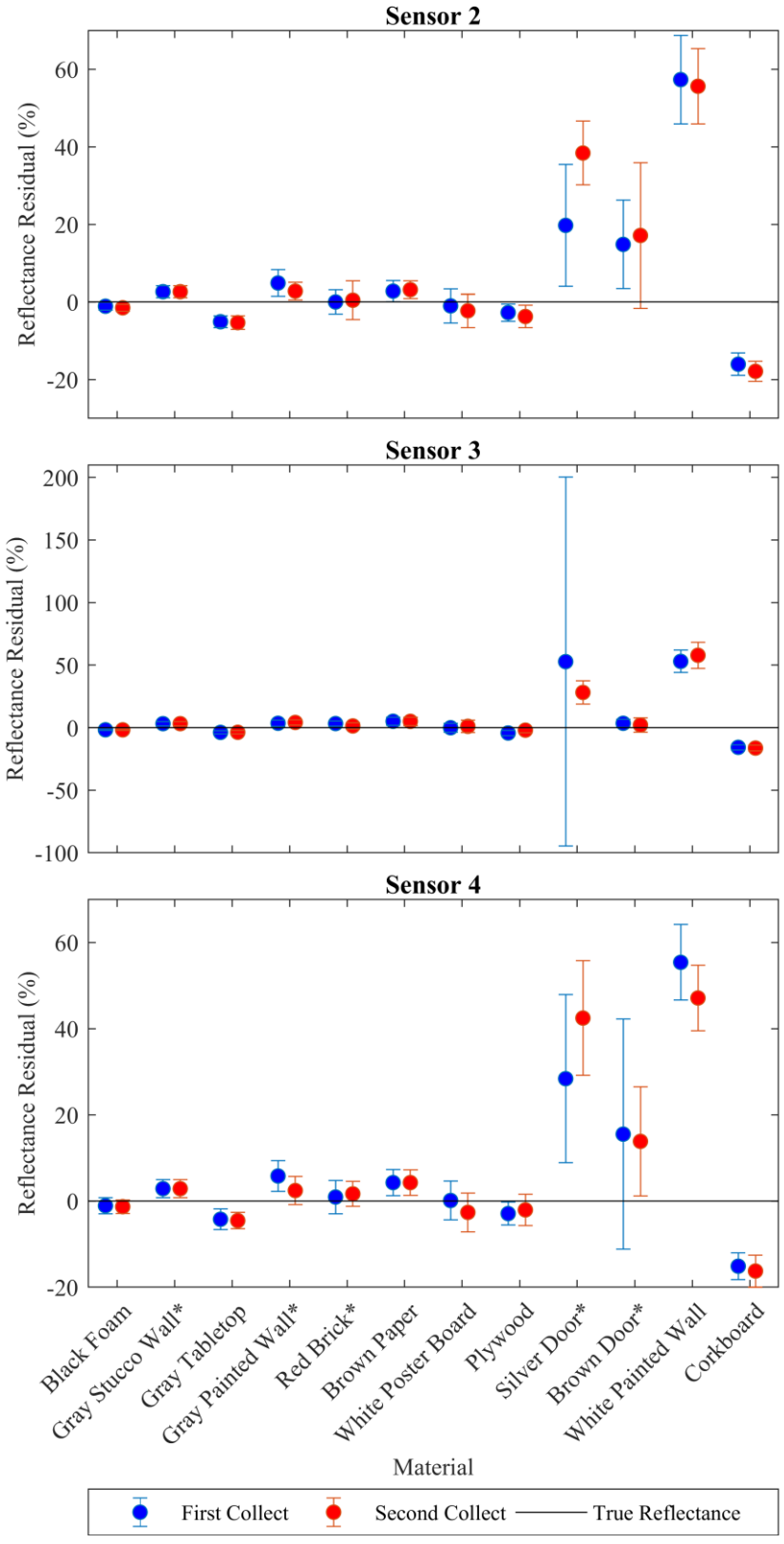

Figure 29 - Temporal Stability for Sensors 2-4